МІНІСТЕРСТВО ОСВІТИ І НАУКИ УКРАЇНИ
НАЦІОНАЛЬНИЙ АВІАЦІЙНИЙ УНІВЕРСИТЕТ
КАФЕДРА КОНСТРУКЦІЇ ЛІТАЛЬНИХ АПАРАТІВ

ДОПУСТИТИ ДО ЗАХИСТУ
Завідувач кафедри д.т.н, проф.
________ Сергій ІГНАТОВИЧ
«___» _________ 2022 р.

ДИПЛОМНА РОБОТА
ВИПУСКНИКА ОСВІТНЬОГО СТУПЕНЯ МАГІСТРА
ЗІ СПЕЦІАЛЬНОСТІ
«АВІАЦІЙНА ТА РАКЕТНО-КОСМІЧНА ТЕХНІКА»

Тема: «Механізм зародження та поширення тріщини під час одновісного стиснення композитів з магнієвою матрицею SiC/AZ91D»

Виконавець:	___________	**Чаоцюнь ЛЯН**
Керівник: к.т.н., доцент	___________	**Володимир КРАСНОПОЛЬСКИЙ**
Охорона праці: к.т.н., доцент	__________	**Катерина КАЖАН**
Охорона навколишнього середовища: к.т.н., доцент	__________	**Леся ПАВЛЮХ**
Нормоконтролер: к.т.н., доцент	__________	**Володимир КРАСНОПОЛЬСКИЙ**

Київ 2022

MINISTRY OF EDUCATION AND SCIENCE OF UKRAINE

NATIONAL AVIATION UNIVERSITY

DEPARTMENT OF AIRCRAFT DESIGN

PERMISSION TO DEFEND
The head of the Department
Professor, Dr. of Sc.
______ Serhiy IGNATOVICH
"___"   ___________2022.

MASTER DEGREE THESIS
ON SPECIALITY
"AVIATION AND SPACE ROCKET TECHNOLOGY"

Topic: "Crack initiation and propagation mechanism during uniaxial compression of SiC/AZ91D magnesium matrix composites"

Fulfilled by:	___________	**Chaoqun LIANG**
Supervisor: **Ph.D., associate professor**	___________	**Volodymyr KRASNOPOLSKY**
Labor protection advisor: **Ph.D., associate professor**	___________	**Katerina KASHAN**
Environmental protection adviser: **Ph.D. associate professor**	___________	**Lesya PAVLYUKH**
Standards Inspector	___________	**Volodymyr KRASNOPOLSKY**

Kyiv 2022

НАЦІОНАЛЬНИЙ АВІАЦІЙНИЙ УНІВЕРСИТЕТ

Факультет аерокосмічний
Кафедра конструкції літальних апаратів
Освітній ступінь «Магістр»
Спеціальність 134 «Авіаційна та ракетно-космічна техніка»
Освітньо-професійна програма «Обладнання повітряних суден»

ЗАТВЕРДЖУЮ
Завідувач кафедри д.т.н., проф.
________ Сергій ІГНАТОВИЧ
«___» ___________ 2022 р.

ЗАВДАННЯ

на виконання дипломної роботи студента

Чаоцюнь ЛЯН

1. Тема роботи «Механізм зародження та поширення тріщини під час одновісного стиснення композитів з магнієвою матрицею SiC/AZ91D», затверджена наказом ректора від 05 жовтня 2022 року №1861/ст.

2. Термін виконання проекту: з 06 жовтня 2022р. по 30 Листопад 2022 р.

3. Вихідні дані до проекту:Параметри AZ91D та SiC, геометрична форма та розміри зразка та основні параметри SiC/AZ91D.

4. Зміст пояснювальної записки: Технічний опис проекту, методи експериментального та чисельного моделювання, 3D кінцеве моделювання композитів SiC/AZ91D, охорона навколишнього середовища та праці.5. Перелік обов’язкового графічного (ілюстративного) матеріалу: презентація Power Point, малюнки та схеми.

Перелік обов’язкового графічного матеріалу: презентація Power point, креслення, діаграми.

6. Календарний план-графік

№ пор.	Завдання	Термін виконання	Відмітка про виконання
1	Створення кінцево-елементної імітаційної моделі композитних матеріалів SiCp/AZ91D.	06.10.2022 – 18.10.2022	
2	Тривимірне моделювання розповсюдження тріщини при стисненні методом кінцевих елементів композитів з різними об’ємними частками.	19.10.2022 – 29.10.2022	
3	Аналогічне моделювання для композитів з різними еквівалентними розмірами частинок.	30.10.2022 – 07.11.2022	
4	Аналогічне моделювання для композитів із різними формами частинок.	07.11.2022 – 10.11.2022	
5	Механічні випробування та випробування мікротвердості, аналіз результатів.	11.11.2022 – 11.12.2022	
6	Виконання розділів охорони навколишнього середовища та праці.	13.11.2022 – 14.11.2022	
7	Оформлення дипломної роботи.	14.11.2022 – 15.11.2022	

7. Консультанти з окремих розділів

Розділ	Консультанти	Дата, підпис	
		Завдання видав	Завдання прийняв
Охорона праці	к.т.н., доцент Катерина КАЖАН		
Охорона навколишнього середовища	к.т.н., професор Леся ПАВЛЮХ		

8. Дата видачі завдання: 5 жовтня 2022 р.

Керівник дипломної роботи: __________ Володимир КРАСНОПОЛЬСКИЙ

Завдання прийняв до виконання: __________ Чаоцюнь ЛЯН

NATIONAL AVIATION UNIVERSITY

Aerospace faculty
Department of Aircraft Design
Educational degree "Master"
Specialty 134 "Aviation and space rocket technology"
Educational professional program "Aircraft equipment"

APPROVED BY
Head of department Dr.Sc., prof.
________ Serhiy IGNATOVICH
"___" ___________ 2022

TASK

For the master degree thesis

Chaoqun LIANG

1. Topic: "Crack initiation and propagation mechanism during uniaxial compression of SiC/AZ91D magnesium matrix composites", approved by the Rector’s order № 1861 "05" October 2022 year.

2. Period of work execution: from 05 October 2022 year to 30 November 2022 year.

3. Initial data: Parameters of AZ91D and SiC, Geometrical shape and dimensions of the specimen, and main parameters of SiC/AZ91D.

4. Content: Technical description of the project, Experimental and numerical simulation methods,3D finite element simulation of SiC/AZ91D composites, and environmental and labor protection.

5. Required material: power point presentation, drawings, and diagrams.

6. Thesis schedule:

№	Task	Time limits	Done
1	Establish a finite element simulation model of SiCp/AZ91D composite materials.	06.10.2022 – 18.10.2022	

2	3D Finite element compression crack propagation simulation of SiCp/AZ91D composites with different volume fractions.	19.10.2022 – 29.10.2022	
3	3D Finite element compression crack propagation simulation of SiCp/AZ91D composites with different equivalent particle sizes..	30.10.2022 – 07.11.2022	
4	3D Finite element compression crack propagation simulation of SiCp/AZ91D composites with different particle shapes.	07.11.2022 – 10.11.2022	
5	Carry out mechanical testings and microhardness testings, and analysis the testing results.	11.11.2022 – 11.12.2022	
6	Implementation of the parts, devoted to environmental and labor protection.	13.11.2022 – 14.11.2022	
7	Edit and correct the draft, and modify the format.	14.11.2022 – 15.11.2022	

7. Special chapter advisers

Chapter	Adviser	Date, signature	
		Task issued	Task received
Labor protection	PhD, associate professor Katerina KAZHAN		
Environmental protection	PhD, professor Lesya PAVLYUKH		

8. Date: 8 September 2022 year.

Supervisor: ___________ Volodymyr KRASNOPOLSKY

Student: ___________ Chaoqun LIANG

РЕФЕРАТ

Пояснювальна записка дипломної роботи магістра «Механізм зародження та поширення тріщини під час одновісного стиснення композитів з магнієвою матрицею SiC/AZ91D»

115 с., 41 рис., 13 табл., 79 джерел

Дана магістерська робота присвячена створенню тривимірних скінченно-елементних моделей для дослідження механізму зародження тріщин і розширення композитів SiC/AZ91D при одновісному стисненні. В роботі до тривимірної моделі SiCp армованих частинками магнієвих матричних композитів (SiCp/AZ91D) було додано одиницю когезійної сили за допомогою кінцево-елементної програми аналізу Abaqus та механізм поширення тріщин SiCp /AZ91D з різними еквівалентними розмірами частинок та об'ємними частками при одновісному стисненні.

Винахід блоку когезійної сили пропонує новий підхід до вирішення проблеми поширення тріщини шляхом уникнення недоліків зразків із заготовленими тріщинами та сингулярності вершини тріщини.

Матеріали роботи можуть бути використані в аерокосмічній промисловості та в освітніх процесах, пов'язаних з деформацією та руйнуванням композитних матеріалів.

Втома, поширення тріщини, когезійна сила, композитні матеріали, скінченно-елементне моделювання, чисельне моделювання

ABSTRACT

Master degree thesis "Crack initiation and propagation mechanism during uniaxial compression of SiC/AZ91D magnesium matrix composites"

115 pages, 41 figures, 5 tables, 79 references

This master thesis is devoted to the creation of three-dimensional finite element models for studying the mechanism of crack initiation and expansion of SiC/AZ91D composites under uniaxial compression. In the work, a unit of cohesive force was added to the three-dimensional model of SiCp particle-reinforced magnesium matrix composites (SiCp/AZ91D) using the finite element analysis program Abaqus and the crack propagation mechanism of SiCp /AZ91D with different equivalent particle sizes and volume fractions under uniaxial compression.

The invention of the cohesive force block offers a new approach to solving the problem of crack propagation by avoiding the drawbacks of pre-cracked specimens and the singularity of the crack tip.

Work materials can be used in the aerospace industry and in educational processes related to the deformation and destruction of composite materials.

Fatigue, crack propagation, cohesive strength, composite materials, finite element modeling, numerical simulation

CONTENTS

INTRODUCTION

As particle-reinforced composites are widely used in the fields of communication, automotive, and aerospace industries, the characterization of composite microstructure, elastic-plastic properties, and especially crack extension failure analysis is particularly important. Numerous studies have found that the introduction of particles not only reduces the ductility and fracture toughness of the material but also may contribute to the generation of microcracks and pores.

The mechanical properties of particle-reinforced metal matrix composites also vary greatly due to many factors, such as the preparation process, the choice of material components, the shape of the reinforcing particles, the equivalent particle size, volume fraction, the degree of bias, and the bonding between the particle and matrix interfaces, among which the effect of particle properties on the properties of composites is particularly significant. Therefore, it is of great academic value to study the particle properties of the crack sprouting and expansion mechanism of particle-reinforced metal matrix composites.

To address this situation, the purpose of this paper is to establish 3D finite element models through numerical simulations to investigate the crack initiation and expansion mechanism of SiC/AZ91D composites under uniaxial compression, and to explore the effects of different particle equivalent particle sizes and different volume fractions of SiC particles on the crack initiation and expansion mechanism of the composites.

1. TECHNICAL DESCRIPTION OF THE PROJECT

1.1 Background and significance of the subject research

Metal Matrix Composites (MMCs) are a new type of material formed by adding inorganic non-metallic (or metallic) reinforcement of different sizes and forms (including fibers, whiskers, particles, nanoparticles, etc.) to a metal matrix as the reinforcing phase by artificial methods[1]. Through reasonable design, metal matrix composites can improve the limitations of poor performance of single-component materials, bring into play the respective performance advantages of the reinforcement and the matrix, and obtain special properties that "alloy" materials do not have, such as high-temperature resistance, high strength, high modulus and low coefficient of thermal expansion, etc., inland transportation, thermal control, aerospace, electronic equipment, sports equipment, and weapons manufacturing. The application potential is huge in the fields of land transportation, thermal control, aerospace, electronic equipment, sports equipment, and weapons manufacturing.

Particles Reinforced Metal Matrix Composites (PRMMCs) are an important part of metal matrix composites, and the commonly used reinforcing particles include oxide ceramics, carbide ceramics, nitride ceramics, such as $A1_20_3$, $Ti0_3$, ZrO_2, SiC, MgO, WC, SiC, Si_3N_4, SiO_2, A1N, B_4C, etc[2]. Particle-reinforced metal matrix composites can be prepared from a variety of matrix alloys and ceramic particles with a wide range of alloy and ceramic particle matching and diverse experimental influencing factors. Therefore, the process of studying the material properties of particle-reinforced metal matrix composites by experimental methods is tedious and costly, and the experimental design cycle is long and has more stringent requirements for personnel operation and equipment. Therefore, in recent years, the prediction and calculation of mechanical properties of particle-reinforced metal matrix composites from theoretical and numerical simulations, followed by experiments to verify the validity of the theoretical and numerical simulation methods, have gradually become one of the common methods for the study of particle-reinforced metal matrix composites[3-5].

As one of the lightest metallic structural materials, the research and utilization of magnesium alloys are receiving more and more attention, but the many disadvantages of magnesium alloys, such as low strength, low modulus, low resistance to wear, low hardness, and high coefficient of thermal expansion, limit its wide application, and magnesium matrix composites can eliminate or mitigate these deficiencies of magnesium alloys [6,7]. Therefore, it is necessary to investigate the relationship between the mechanical damage mechanism and various influencing factors of magnesium matrix composites, so that it can effectively provide a reliable theoretical basis and guarantee for the application and development of composite materials.

1.2 The current state of research

In the fields of communication, automotive, and aerospace sectors, the research of the deformation and fracture behavior of particle-reinforced metal matrix composites has vital applications[8,9]. The conventional strength design assumes that the material is a continuum without defects, and the failure process is divided into three stages: crack initiation, crack propagation, and fracture. But in fact, there are always crack defects in materials. Therefore, the application of fracture damage mechanics theory to fatigue strength design is the trend of future development.

Numerous facts[10-12] have demonstrated that low-stress fracture caused by crack extension is the underlying factor in a wide range of structural and component failures as well as a wide range of significant incidents in engineering. The need to learn about numerous crack emerging events, comprehend the crack expansion circumstances, and comprehend the crack expansion mechanism led to the gradual emergence and development of fracture mechanics. An important theoretical foundation for estimating the strength and predicting the lifespan of engineering components is fracture mechanics. Fracture mechanics has played a significant role in assisting people in understanding the full range of crack extension, from the microscopic scale of atomic dislocations to the macroscopic process of crack extension, from the deformation fracture in the linear elastic phase to the energy change in the elastic-plastic zone[13].

In fracture mechanics, cracks can be divided into three ways according to the expansion mode of cracks under the action of external force, as shown in Fig. 1.1:

(1) Open type (Model I): The crack produces an opening displacement under the action of tensile stress perpendicular to the crack surface.

(2) Sliding type (Model II): The crack produces a sliding displacement under the action of shear stress perpendicular to the crack front.

(3) Tear-off type (Model III): The crack produces a tear-off displacement under the action of shear stress parallel to the crack front.

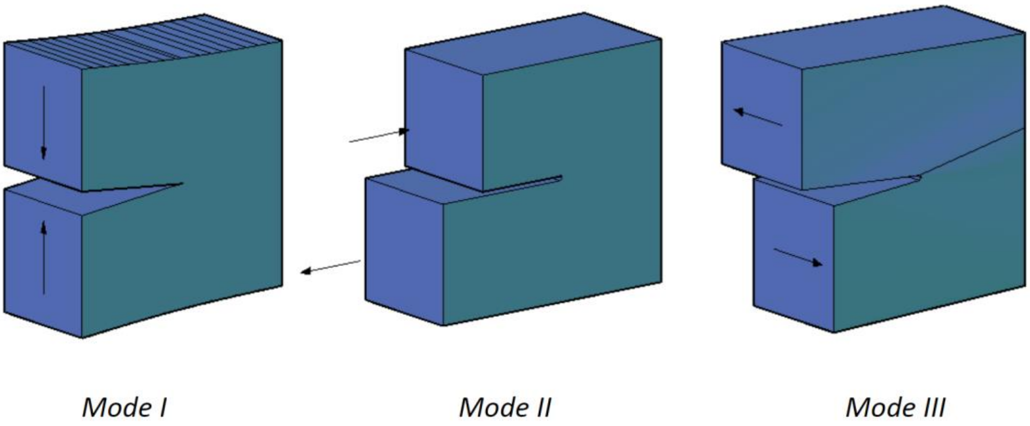

Fig. 1.1. Three basic forms of cracks.

The model I, II, and III cracks are all for penetrating cracks, and type I cracks are the main damage in engineering practice [14].

Numerous studies [15-19] have discovered that a variety of factors, including the preparation method, the selection of material components, the shape of the reinforcing particles, equivalent particle size, volume fraction, degree of bias aggregation, and bonding at the interface between the particles and the matrix, among others, can greatly affect the mechanical properties of particle-reinforced metal matrix composites. Studying the effects of particle characteristics on the crack expansion and sprouting mechanisms of particle-reinforced metal matrix composites is therefore extremely valuable academically.

Particle-reinforced metal matrix composites are most commonly damaged by the particles themselves breaking, the particle-matrix contact debonding, and the matrix failing [15]. By using the powder cure (PM) method, Peng [16] created B_4C_p/6061A1 composites with various particle sizes. He then observed the crack expansion in the composites and discovered that the damaged interface and fractured particles act as the initial crack, expand along the high-strain region of the matrix at the crack's tip, and eventually form the main crack. When Rahimian and Ehsani et al. [17] looked at the mechanical characteristics of Al_2O_3-reinforced composites with various particle sizes, they discovered that larger reinforcing particles increased the matrix's grain size and were more likely to fracture during hot pressing, which increased the composite's porosity. In their investigation of the impact of particle form on the microstructure and mechanical characteristics of SiC_p/Al composites, Cui Yan et al. [18] discovered that the composites are more vulnerable to fracture and exhibit greater stress concentration at the sharp corners of the particles. Additionally, Li Kun et al [19] looked at how SiC particle volume fraction affected the spreading of fatigue crack prevention in SiC_p/A1 composites. The findings indicated that as the volume percent of SiC particles was increased, the fatigue fracture propagation resistance of the composites grew as well. However, it was only at 15% that the fatigue crack propagation resistance of the composites exceeded that of the matrix.

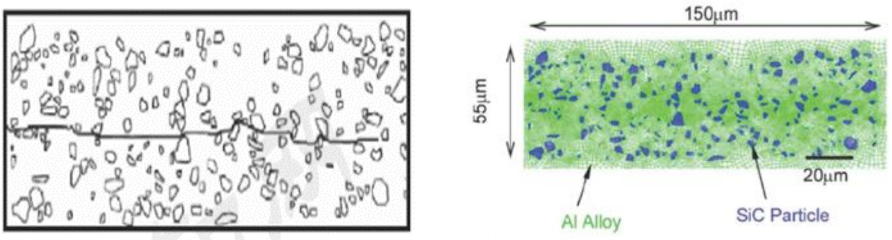

Fig. 1.2. SiC-Al crack propagation path.

Numerical simulation techniques are another significant means to examine the mechanical damage properties of composites, in addition to experimental research methods. Many researchers [20-23] have simplified the reinforcing particles into ideal shapes to create corresponding three-dimensional finite element models to study the impact of particle microscopic properties on the crack sprouting and extension mechanism of composites. For instance, Azra Rasool et al. [20] built 3D finite element models to explore the impact of particle form on the macro and micro fracture behavior of composites by simplifying the particles into spherical, square, and ortho-octahedral shapes.

To study the impact of mixed particles on the fracture behavior of iron matrix composites, Liu Peng [21] simplified the particles to a spherical shape and established TiC and TiN particles in mixed reinforced iron matrix composites. Due to the disregard for the microscopic characteristics of the composites' reinforcing particles, there are significant discrepancies between the simulation findings and the actual outcomes. To implement a 3D finite element simulation, it is currently standard practice to create the matching finite element model of the composite material based on the microstructure of the reinforcing particles. For instance, Su et al [22] established a 3D finite element model of the microscope structure of the approximate shape of SiC particles and studied the effect of SiC particle properties on the fracture behavior of metal matrix composites. Zhang et al [23] studied the fracture mechanism of SiC/Al composites during the tensile process by doing the same.

In conclusion, aluminum alloy is typically used as the matrix by researchers looking at the effects of particle characteristics on the fracture mechanism of metal matrix composites [16-23], while magnesium alloy-based composites are much less frequently documented.

1.3 Numerical simulation of crack expansion

With the rapid development of computer technology, numerical computational methods have a unique advantage in the study of particle-reinforced composites and are increasingly favored by researchers. The current simulation methods for crack extension include the SMART method (Separating, Morphing, Adaptive and Remeshing Technology); VCCT-based crack extension (virtual crack closure technique); cohesive zone model(CZM) to simulate fracture; and extended finite element method(XFEM). Among them, the most frequently used are the extended finite element method based on the finite element method and the cohesive zone model method, which are based on the theory of linear elastic fracture mechanics and elastoplastic fracture mechanics, respectively, and have their advantages and differences in the simulation of crack extension problems.

1.3.1 Extended finite element (XFEM)

In 1999, Belytschko [24] proposed the extended finite element method (XFEM) for solving discontinuities in the conventional finite element framework. This method is based on the idea of unit decomposition and the addition of the jump function and the crack tip progressive displacement field function to the conventional finite element model, and the finite element mesh is independent of the crack. Mose et al [25] simulated the expansion path of arbitrary cohesive cracks in concrete materials by using extended finite elements. In the literature [26-27], surface dislocations in arbitrary materials were simulated. In this paper, the displacement mode of the extended finite element is given for type I cracks, the discrete equations are developed, the detailed procedure of calculating the stress intensity factor by J-integration is derived, and the influence of the integration area and mesh density on the accuracy of the stress intensity factor calculation is analyzed.

The basic principles of the extended finite element method are.

(1) Construction of displacement mode

The displacement pattern in the conventional finite unit method is expressed as

$$u(x) = \sum_{i=1}^{n} N_i u_i \tag{1}$$

where: N_i is the interpolated shape function of node i; u_i is the displacement vector of node i. At any point in the domain, the interpolated shape function satisfies $\sum_{i=1}^{n} N_i\,(x,y) = 1$. However, the displacement mode of the above formula for conventional finite elements is only applicable to continuous media and is not suitable for dealing with discontinuities such as cracks.

Belytschko et al.[26] of Northwestern University proposed an approximate displacement interpolation function suitable for describing crack-containing surfaces based on the idea of unit decomposition of the interpolation function.

$$u(x) = \sum_{i\in N} N_i(x)u_i + \sum_{j\in N^{dic}} N_j H(x)\alpha_j + \sum_{k\in N^{asy}} N_k \sum_{\alpha=1}^{4} \phi_\alpha(x)\, b_k^\alpha \tag{2}$$

where: N is the set of all conventional unit nodes; N^{disc} is the set of unit nodes completely penetrated by cracks (nodes indicated by the square in Fig. 1.3); N^{asy} is the set of unit nodes containing crack tips (nodes indicated by the circle in Fig. 1.4); u_i,α_j, b_k^α denote the displacements of conventional unit nodes, penetration unit nodes and crack tip unit nodes, respectively; H(x) is the jump function (Heaviside function, Eq. 3), is used to reflect the discontinuity of the crack surface displacement, on the crack surface, the lower side is taken as +1 and -1, respectively.

$$H(x) = \begin{cases} +1 & \text{Crack face side} \\ -1 & \text{Lower side of crack surface} \end{cases} \tag{3}$$

$\phi_\alpha(x)$ is an additional function of the crack tip asymptotic displacement field, reflecting the stress singularity of the crack tip, and consists specifically of the following basis functions.

$$\phi_\alpha(x) = \left[\sqrt{r}sin\frac{\theta}{2}, \sqrt{r}cos\frac{\theta}{2}, \sqrt{r}sin\frac{\theta}{2}cos\theta, \sqrt{r}cos\frac{\theta}{2}cos\theta\right] \tag{4}$$

where: r, θ is the polar coordinate system with the crack tip as the coordinate origin (Fig. 1.4).

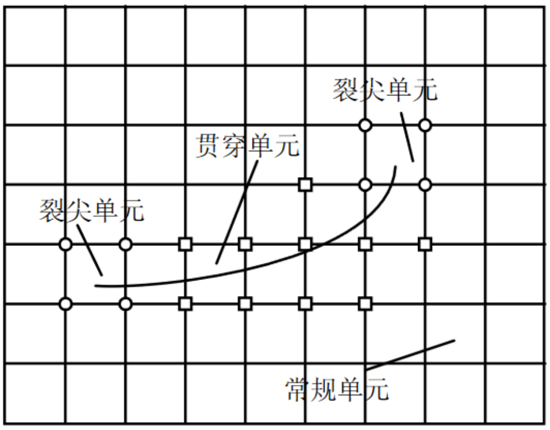

Fig. 1.3. Additional Functions for Enhanced Nodes

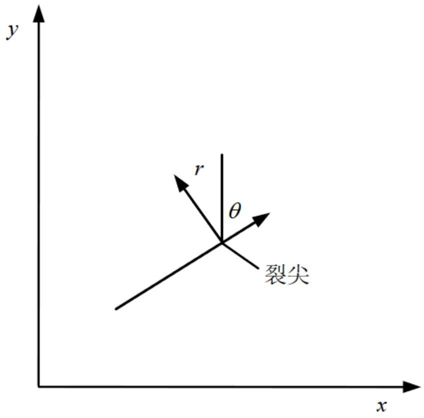

Fig. 1.4. Crack tip coordinate system.

(2) Establishment of discrete equations

As with conventional finite elements, substituting the finite element approximation displacement function (1) into the imaginary work equation yields the discrete equation.

$$Kd = F \tag{5}$$

Where K is the overall stiffness matrix, integrated by the cell stiffness matrix:

$$k_{ij}^{e} = \begin{pmatrix} k_{ij}^{uu} & k_{ij}^{ua} & k_{ij}^{ub} \\ k_{ij}^{au} & k_{ij}^{aa} & k_{ij}^{ab} \\ k_{ij}^{bu} & k_{ij}^{ba} & k_{ij}^{bb} \end{pmatrix} \tag{6}$$

Among them:

$$k_{ij}^{rs} = \int_{\Omega} (\boldsymbol{B}_i^r)^T D B_j^s \, d\Omega, (r, s = u, a, b) \tag{7}$$

B_i^r is the partial derivative of the form function (B_i^u, B_i^α, B_i^b correspond to the regular cell, the split-tip cell through the cell Split-tip cell), which is expressed as follows:

$$\left.\begin{aligned} B_i^u &= \begin{bmatrix} N_{i,x} & 0 \\ 0 & N_{i,y} \\ N_{i,y} & N_{i,x} \end{bmatrix} \\ B_i^\alpha &= \begin{bmatrix} (N_i H)_{,x} & 0 \\ 0 & (N_i H)_{,y} \\ (N_i H)_{,y} & (N_i H)_{,x} \end{bmatrix} \\ B_i^b &= \begin{bmatrix} (N_i \phi_\alpha)_{,x} & 0 \\ 0 & (N_i \phi_\alpha)_{,y} \\ (N_i \phi_\alpha)_{,y} & (N_i \phi_\alpha)_{,x} \end{bmatrix} \ (\alpha = 1\sim4) \end{aligned}\right\} \tag{8}$$

d is the nodal displacement vector, which includes the displacements of the regular unit nodes, crack penetration unit nodes and crack tip unit nodes.

$$d = \left\{u_i, a_i, b_i^1, b_i^2, b_i^3, b_i^4\right\}^T \tag{9}$$

F is the equivalent nodal load vector, which is formed by the collection of equivalent nodal loads of each unit (see fig.1.5). denotes the equilibrium state of the object under the boundary conditions, $\Gamma_t, \Gamma_u, \Gamma_c$ are the external force boundary, displacement boundary, and crack boundary respectively; f_t, f_b denote the body force and external force respectively.

$$F = \left\{f_i^u, f_i^a, f_i^{b1}, f_i^{b2}, f_i^{b3}, f_i^{b4}\right\}^T \tag{10}$$

Among them:

$$\left.\begin{aligned} f_i^u &= \int_{\Gamma_t} N_i f_t d\Gamma + \int_\Omega N_i f_t d\Omega \\ f_i^a &= \int_{\Gamma_t} N_j H f_t d\Gamma + \int_\Omega N_j H f_t d\Omega \\ f_k^{ba}\Big|_{a=1,2,3,4} &= \int_{\Gamma_i} N_k \phi_\alpha f_t d\Gamma + \int_\Omega N_j \phi_\alpha f_b d\Omega \end{aligned}\right\} \tag{11}$$

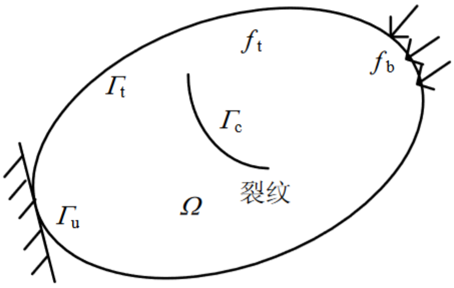

Fig. 1.5. Boundary equilibrium state.

1.3.2 Cohensive Zone Model (CZM)

The cohesive Zone Model (CZM), which is seen in fig. 1.6, was initially presented by Dugdale and Barenblat[28] to reduce the stress singularity at the crack tip. The Cohesive Zone Model was first put forth, and since then it has been extensively utilized to examine a variety of composite materials, including interface delamination, adhesive interface cracking, and fracture of quasi-brittle materials like ductile metals.

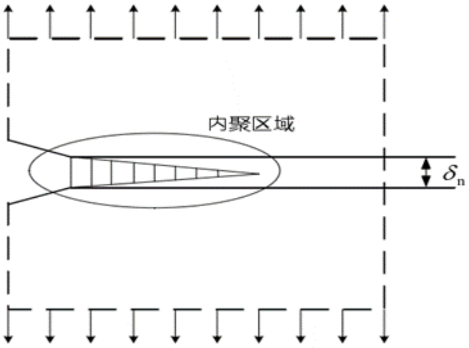

Fig. 1.6. Crack tip cohesion region.

Needleman[29] proposed a nonlinear cohesion model in quadratic polynomial and exponential form (i.e. parabolic) to analyze the cracking of grains in metals and the dynamic expansion of grain cracks with bubbles; Tvergaard and Hutchinson [30] proposed a trilinear cohesion model for elasticity and ideal plasticity; Camacho and Ortiz [31] proposed a bilinear cohesion model for brittle fracture and used this cohesion model to simulate the crack expansion of a two-armed beam specimen under impact loading; Geubelle and Baylor [32] used a bilinear cohesion model to simulate the crack initiation, extension and delamination of composite fiber plates under low-velocity impact loading. The above-calculated results compared well with the experimental results, and all of them reflected the actual fracture characteristics. Different shapes of cohesion models correspond to different tensile-disintegration intrinsic relationships, where the main fracture parameters are critical stress and fracture energy, while the shape parameters determine the shape of the cohesion model (parabolic, bilinear and trilinear) and its mechanical properties[33-35]. The fracture energy of the cohesion model was obtained by theoretical calculations and experimental comparisons. The mechanical properties of fracture and crack emergence of the cohesion model were obtained using theoretical calculations and experimental comparisons. for the analysis of the reliability of different bonding materials and bonding structures under actual working conditions. reliability [36-41] .

Although, Blackman et al [42] concluded that the shape parameters of the cohesion model are independent of the fracture curve during the fracture of a two-armed beam, Yan and Shang [43] calculated that the shape parameters of the cohesion model play a role in their analysis. Recently, researchers[44-46] have started to focus on the effect of the shape and important parameters of the cohesion model on the modeling of different adhesives and bond structures; Campilho et al.[47,48] showed that the shape of the cohesion model has a significant effect on the lap structure of ductile adhesive bonds, but not on brittle adhesives.

The influence of the shape of the cohesion model on the lap structure of ductile adhesives was significant, but not on brittle ones.

As shown in Fig. 1.7, there are three commonly used traction-separation-based modeling damage initiation-evolution criteria: Bilinear, Exponential, and Trapezoidal.

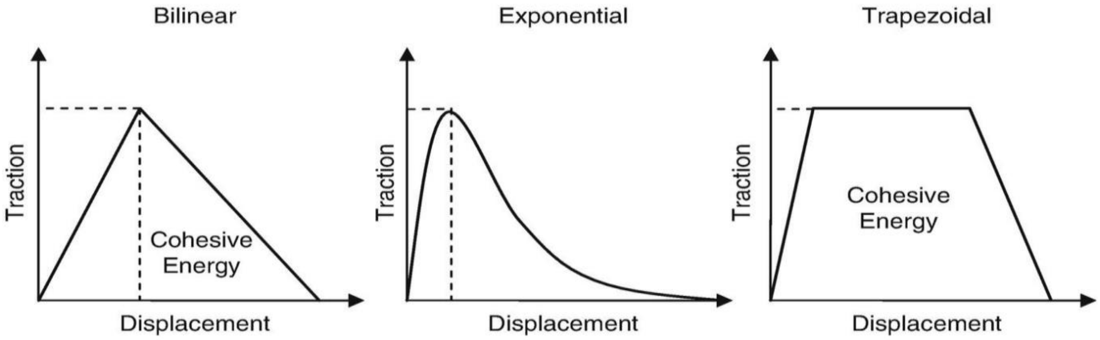

Fig. 1.7. Three traction separation criteria.

(1) Bilinear cohesive model

The relationship between the tensile force and the separation displacement of the bilinear cohesion model is given by

$$T_n = \begin{cases} \frac{\sigma_{max}}{\sigma_{n1}} \Delta_n & (\Delta_n \le \sigma_{n1}) \\ \sigma_{max} \frac{\delta_n^f - \Delta_n}{\delta_n^f - \delta_{n1}} & (\Delta_n > \sigma_{n1}) \end{cases} \tag{12}$$

$$T_\tau = \begin{cases} \frac{\sigma_{max}}{\sigma_{\tau 1}} \Delta_\tau & (\Delta_\tau \le \sigma_{\tau 1}) \\ \sigma_{max} \frac{\delta_\tau^f - \Delta_\tau}{\delta_\tau^f - \delta_{\tau 1}} & (\Delta_\tau > \sigma_{\tau 1}) \end{cases} \tag{13}$$

Tensile and shear fracture energy is

$$\phi_n = \frac{1}{2} \sigma_{max} \delta_n^f \tag{14}$$

$$\phi_\tau = \frac{1}{2} \tau_{max} \delta_\tau^f \tag{15}$$

Where δ_n^f and δ_τ^f are the critical displacements for the interface separation and also the bilinear shape parameters of the model, as shown in Fig. 1.7.

(2) Exponential cohesive model

The relationship between the tensile force and the separation displacement for the cohesion model in exponential form is given by

$$T_n = -\frac{\phi_n}{\delta_{n1}} \exp(-\frac{\Delta_n}{\delta_n}) \left\{\frac{\Delta_n}{\delta_n} \exp\left(-\frac{\Delta_\tau^2}{\delta_{\tau1}^2}\right) + \frac{1-q}{r-1}\left[1 - exp\left(-\frac{\Delta_\tau^2}{\delta_{\tau1}^2}\right)\right]\left(r - \frac{\Delta_n}{\delta_{n1}}\right)\right\} \quad (16)$$

$$T_\tau = -\frac{\phi_n}{\delta_{n1}} 2 \frac{\delta_{n1}}{\delta_{\tau1}} \frac{\Delta_\tau}{\delta_{\tau1}} \left[q + \left(\frac{r-q}{r-1}\right) \frac{\Delta_n}{\delta_{n1}}\right] exp\left(-\frac{\Delta_n}{\delta_{n1}}\right) exp\left(-\frac{\Delta_\tau^2}{\delta_{\tau1}^2}\right) \quad (17)$$

The fracture energies in tension and shear are associated with the critical stresses and are expressed as

$$\phi_n = \sigma_{max}\sigma_{n1}e \quad (18)$$

$$\phi_\tau = \sqrt{e/2}\,\tau_{max}\delta_{\tau1} \quad (19)$$

where T_n and T_τ are the tensile and shear forces; ϕ_n and ϕ_τ are the separation work in tensile and shear, respectively; Δ_n and Δ_τ are the separation work in tensile and shear, respectively. σ_{max} and τ_{max} are the critical stresses for tensile and shear fractures.σ_{n1} and $\delta_{\tau1}$ are the displacements when the tensile and shear stresses reach the critical stresses, respectively;$q = \phi_\tau/\phi_n$,$r = \Delta_n^*/\delta_{n1}$.

(3) Trapezoidal cohensive model

The relationship between the tensile force and the separation displacement of the trapezoidal cohesion model is given by

$$T_n \begin{cases} \& \frac{\sigma_{max}}{\sigma_{n1}} \Delta_n & (\Delta_n \leq \delta_{n1}) \\ \sigma_{max} & (\delta_{n1} \leq \Delta_n \leq \delta_{n2}) \\ \frac{\sigma_{max}}{\delta_n^f - \delta_{n2}} \left(\delta_n^f - \Delta_n\right) & (\delta_{n2} \leq \Delta_n \leq \delta_n^f) \\ 0 & (\Delta_n > \delta_n^f) \end{cases} \quad (20)$$

$$T_\tau \begin{cases} \frac{\tau_{max}}{\sigma_{\tau 1}} \Delta_\tau & (\Delta_\tau \leq \delta_{\tau 1}) \\ \tau_{max} & (\delta_{\tau 1} \leq \Delta_\tau \leq \delta_{\tau 2}) \\ \frac{\tau_{max}}{\delta_\tau^f - \delta_{\tau 2}} \left(\delta_\tau^f - \Delta_\tau\right) & (\delta_{\tau 2} \leq \Delta_\tau \leq \delta_\tau^f) \\ 0 & (\Delta_\tau > \delta_\tau^f) \end{cases} \tag{21}$$

The fracture energy of tensile and shear for this cohesion model is

$$\phi_n = \frac{1}{2}\sigma_{max}\left(\delta_{n2} - \delta_{n1} + \delta_n^f\right) \tag{22}$$

$$\phi_\tau = \frac{1}{2}\tau_{max}\left(\delta_{\tau 2} - \delta_{\tau 1} + \delta_\tau^f\right) \tag{23}$$

Where $\delta_{n1}, \delta_{n2}, \delta_n^f, \delta_{\tau 1}, \delta_{\tau 2}$, and δ_τ^f are the separation displacements corresponding to the different stresses of the cohesion model, respectively, and are the shape parameters of the trilinear cohesion model.

Summary of this chapter

Chapter 1 is the introduction, which mainly introduces the background and significance of the topic selection of the paper, as well as the latest progress of related research at home and abroad, and defines the research content and research methods of this paper.

2. EXPERIMENTAL AND NUMERICAL SIMULATION METHODS

2.1 Experimental material preparation and testing

(1) Experimental materials

The experimental materials were commercial α-SiC particles with equivalent particle sizes of 5 μm, 10 μm, and 15 μm. The composition of magnesium alloy AZ91D is shown in table 2.1.

In this experiment, the main experimental equipment needed is: medium frequency induction resistance melting furnace, medium frequency induction insulation preheating furnace, electric furnace temperature control equipment, gas protection device, graphite casting mold, thermocouple thermometer, metallographic polishing machine, metallographic microscope, tungsten filament scanning electron microscope, microelectronic universal mechanical testing machine. Auxiliary experimental equipment is: file, manual saw, bench vise, crucible, burning fire brick, graphite stirring bar, crucible pliers, pulling spoon, funnel, heat-proof gloves, brush, etc.

Table 2.1

Composition of AZ91D magnesium alloy for experimental use(*wt*%)

Element	Mg	Al	Zn	Mn	Si	Cu	Ni	Fe	Be
wt%	balance	8.9504	0.6326	0.2614	0.0223	0.0018	0.0005	0.0023	0.0003

(2) The preparation process of the experiment

The preparation of magnesium matrix composites by all-liquid stir casting is prepared by:

① Prepare the alloy material. Use sandpaper or a file to polish off the dirt and oxide layer on the surface of the material. If the material is large, use a hydraulic press to divide it into small pieces (at least smaller than the diameter of the crucible).

② Preparation of crucible. The experiments were performed with a small stainless steel crucible, so the crucible must be cleaned and preheated to 250°C before heating the crucible to prevent impurities such as iron filings within the crucible wall from being incorporated into the alloy solution.

③ Preheating. Magnesium alloy will be a violently exothermic reaction when it meets water, so all experimental materials and equipment that need to contact with magnesium alloy solution must be baked dry and preheated to 250℃ in preheated resistance furnace, such as alloy materials, molds, graphite stirring bars, crucible tongs, plucking spoons, funnels, etc. SiC particles with equivalent particle sizes of 0um, 5um, 10um, and 15um were cleaned and dried in alcohol, wrapped in aluminum foil, and preheated at 600°C (volume fractions of 0%, 5%, 10%, and 15%)

④ Preparation of paint and brushing paint. First prepare the paint (mixture, the mass ratio is water: water glass: talc = 3:1:3), and then preheat to 250 ℃ crucible wall, crucible pliers, plucking spoons, funnel and other iron products surface are brushed with a uniform thickness of paint, and finally put back to the preheating furnace, baked dry and insulation 250℃.

⑤ When ready for all the above work, it will start the alloy melting, it should be noted that: magnesium alloy melting the whole process, is required to mix gas

($99vol.\%CO_2+1vol.\%C_2F_6$) protection, block all possible contact between magnesium alloy solution and air.

The preparation process of magnesium matrix composites by all-liquid stir casting is as follows:

① Heating crucible. Put the clean, painted, preheated 250°C crucibles into the medium frequency induction resistance melting furnace, set the heating temperature to 400°C, and heat the crucible to dark red.

② Melting magnesium alloy. Put the preheated AZ91D magnesium alloy into the dark red crucible, set the heating temperature to 740℃, and heat the magnesium alloy to the liquid metal state.

③ Add flame retardant and SiC particles. When the magnesium alloy is completely melted into the state of metal liquid, add 0.4vol.% of flame retardant Ca into the metal liquid, cool to 670℃, add the aluminum foil-wrapped SiC particles into the molten metal liquid, stir rapidly clockwise for 2-5min, and then keep warm for 10min.

④ Stirring. The metal liquid was cooled to 585°C and semi-solid mechanical stirring was carried out for 30 min at 400 r/min; after that, the temperature was increased to 720°C and liquid mechanical stirring was carried out for 5 min at 400 r/min to ensure that the SiC particles could be uniformly distributed in the metal liquid.

⑤ Slag picking and temperature measurement. Pick off the oxidized skin on the surface of the alloy liquid with a pulling spoon and a funnel, stir the metal liquid clockwise again with the pre-heated graphite rod, and measure and control the temperature of the solution to reach the pouring temperature.

⑥ Pouring and molding. Cool to near liquid phase line temperature of 595°C, hold for 10 minutes to get a semi-solid embryo, use crucible clamp to clamp the crucible out of the resistance furnace, and quickly pour into 200°C preheated mold for molding.

⑦ Extrusion casting. The prepared semi-solid embryo was put into the semi-solid extrusion die (shown in fig. 2.1), put into the open and closed furnace at 585°C for 30 min, extrusion pressure 2000KN, extrusion speed 1mm/s, holding pressure for 1 min, and the specimen was removed after forming and cooling (shown in fig. 2.2).

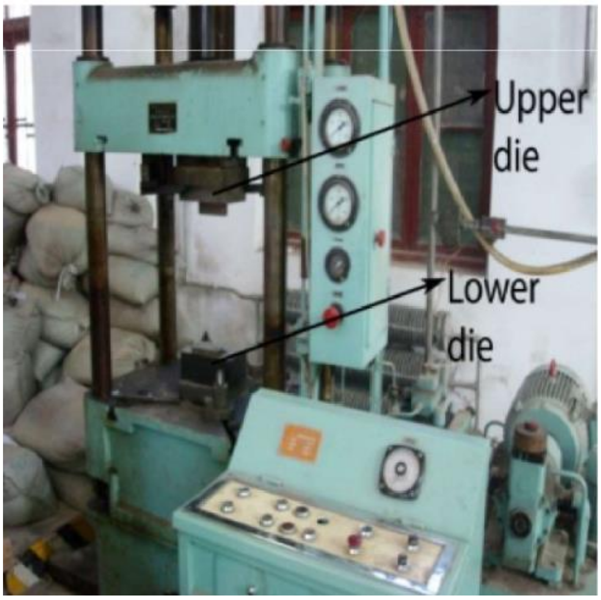

Fig. 2.1. 13YB32-100B four-column presses machine.

Fig. 2.2. SiC$_p$/AZ91D composite casting.

2.1.1 Mechanical performance testing

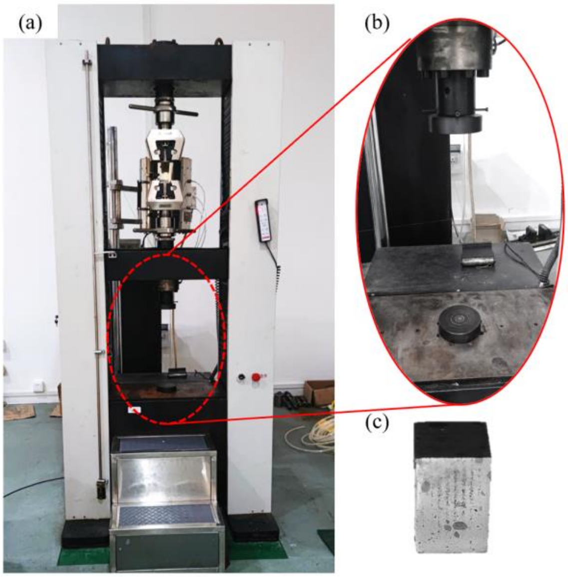

Fig. 2.3. Microelectronic universal mechanical testing machine.

WDW-E100D microelectronic universal testing machine was used for room temperature compression experiments on magnesium matrix composites, the specimen was a rectangular body of 8 mm×8 mm×12 mm, the loading rate was 0.2mm/min, and continuous loading was used until the composite specimen was fractured, the original data was kept and plotted into compression stress-strain curve.

2.1.2 Microstructure observation

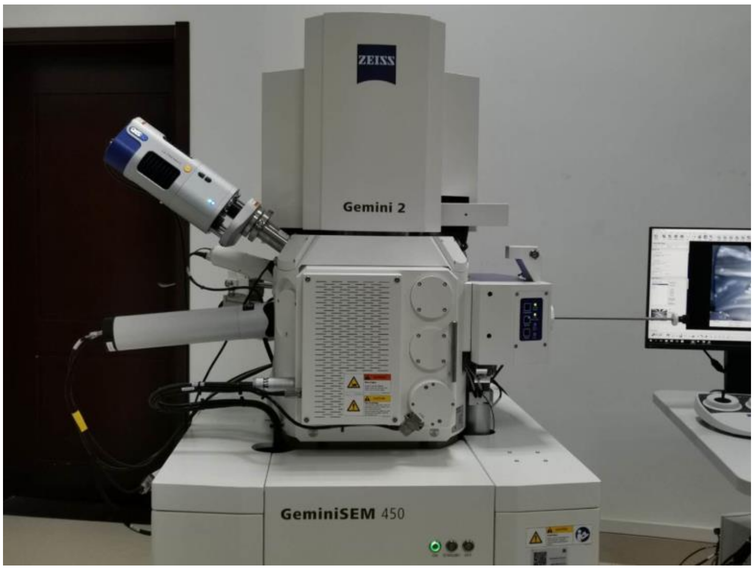

Fig. 2.4. Field emission scanning electron microscope

Field emission scanning electron microscope (FESEM) is composed of an electron optical system, signal collection and processing, image display and recording system, and vacuum system. The electronic image of the field emission scanning electron microscope is very sensitive to the four convexities of the specimen surface, which can show the organization and morphology of the fracture specimen surface. After the sintering of magnesium matrix composite materials selected 400#, 600#, 800#, 1500#, and 2000# sandpaper to coarse grinding to fine grinding, pay attention to each with sandpaper grinding, the specimen rotated 90 ° to ensure that each sandpaper abrasion marks perpendicular to each other, in time to observe whether the previous layer of coarse abrasion marks has been eliminated, the grinding process is water grinding. Next, the specimen is polished until the surface of the specimen is free of scratches and etched with a 2% nitric acid alcohol solution. After the etching process, the specimens were cleaned with alcohol and then dried with a hair dryer on the cold air setting. In this study, the fracture morphology of the tensile specimens was observed using an FEI Nova Nano SEM450 field emission scanning electron microscope (SEM) with an accelerating voltage of 200 V-30 kV.

2.2 Numerical simulation methods

2.2.1 Model building method

In this paper, SiC particles with equivalent particle sizes of 5, 10, 15, and 20 μm were selected, and the basic parameters of AZ91D magnesium alloy and SiC particles are shown in table 2.2 [49,50].

Table.2.2

Basic parameters of AZ91 magnesium alloy and SiC particles

Material	$\rho/(Kg/m^3)$	E/GPa	μ	σ_b/MPa
AZ91D	1800	45	0.33	164
SiC	3215	450	0.17	2000

Note:ρ is the material density; E is the modulus of elasticity; μ is Poisson's ratio; $\sigma_b$is the tensile strength.

Fig. 2.5 (a) shows the SEM image of SiC particles, and fig. 2.5 (b) shows the enlarged red area in fig. 2.5 (a), from which it can be seen that the original shape of SiC particles is mostly irregular polyhedra [51], so the shape of SiC particles is designed as irregular polyhedra in 3D simulation, as shown in fig. 2.5 (c).

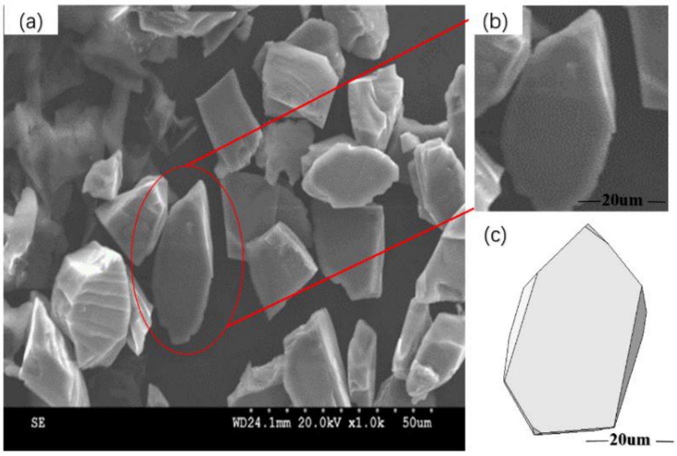

(a) SEM image of SiC particles (b) Actual morphology of SiC particles

(c) Regenerated particle model

Fig. 2.5. The actual morphology of SiC particles and its modeling.

The RSA stochastic algorithm (see Appendix for the algorithm procedure) was used to randomly deposit 2D and 3D particles in the metal matrix without overlapping each other. This resulted in three 3D finite element models of the composites, the first model with square, true shape, and round particle shapes and 15% volume fraction; the second model with particle equivalent particle sizes of 5, 10, 15, and 20 μm and 15% volume fraction; the third model with particle equivalent size of 10 μm and particle volume fractions of 5%, 10%, 15%, and 20%, respectively.

2.2.2 Constitutive behaviors

(1) Matrix Constitutive behavior

Abaqus can represent the constitutive model of the AZ91D matrix in SiCp/AZ91D composites with various methods, such as Isotropic, Kinematic, and Johnson-Cook. Among them, the Johnson-Cook model can process the plastic stress and strain curves obtained in the experiment into functions and describe the plasticity of materials, which can well explain the changes occurring at this crack growth stage. Therefore, the Johnson-Cook model is adopted as the constitutive model of the AZ91D matrix in this paper. Where the expression [52] is:

$$\sigma = A + B\varepsilon^{n}\left[1 + Cln\left(1 + \frac{\varepsilon}{\varepsilon_0}\right)\right](1 - T^{*m}) \tag{24}$$

Since this paper is carried out at room temperature, the influence of temperature softening and strain rate hardening on stress can be ignored, so the formula is simplified as follows:

$$\sigma = A + \mathrm{B}\varepsilon^{n} \tag{25}$$

Where A is the yield strength of the AZ91D matrix under static load, B is the hardening coefficient, and N is the hardening index. In the hardening stage, the plastic strain accumulates continuously. When the total accumulated strain meets a specific value, the crack begins to expand.

The crack begins to expand, and the strain continues to increase. When the stress reaches a specific value, it begins to decrease. Assuming that the damage variable changes linearly with the plastic displacement, the failure displacement is set, and the expression D of the stiffness damage [53] is:

$$D = \frac{L\varepsilon^{\mathrm{pl}}}{u_f^{\mathrm{pl}}} = \frac{u^{\mathrm{pl}}}{u_f^{\mathrm{pl}}} \tag{26}$$

The B hardening coefficient and n hardening index of the magnesium alloy matrix were obtained by reference [54], and the yield strength of AZ91D magnesium alloy under static load was 164MPa, the hardening coefficient was 600MPa, the hardening coefficient n was 0.283, and the failure displacement was 0.00015, as shown in *Table 2.3*.

Table 2.3

Johnson-Cook (J-C) constitutive model parameters for AZ91D magnesium alloy

A/MPa	B/MPa	n	C	u_f^{pl}
164	600	0.283	0.021	0.00015

Notes: A is the yield strength of AZ91D matrix under static load; B is the hardening constant; n is the hardening exponent; C is the strain rate constant; u_f^{pl} is the failure displacement.

(2) Particle Constitutive Behavior

The elastic response and brittle fracture behavior of SiC particles are described by the ABAQUS/Explicit brittle fracture model. In brittle fracture, an initial crack is formed when the maximum principal stress received by the material exceeds the fracture strength of the material, which is expressed as follows：

$$G_c = \rho\left(e_{\mathrm{nn}}^{\mathrm{ck}}\right)G \tag{27}$$

Where G_c is the shear modulus of the damage process, G is the initial shear modulus of the material, $\rho(e_{nn}^{ck})$ is the damaged strain function and the relationship with the damaging strain $e_{\mathrm{nn}}^{\mathrm{ck}}$ is [55] :

$$\rho\left(\mathrm{e}_{\mathrm{nn}}^{\mathrm{ck}}\right) = \left(1 - \frac{\mathrm{e}_{\mathrm{nn}}^{\mathrm{ck}}}{\mathrm{e}_{\mathrm{max}}^{\mathrm{ck}}}\right)^{\mathrm{p}} \tag{28}$$

Where $e_{\mathrm{max}}^{\mathrm{ck}}$ and P are material parameters.

Since silicon carbide is powdered primarily, it is not easy to test its compression experiment. Therefore, this paper quotes the experimental parameters provided by reference

[23] to define the brittle constitutive model of silicon carbide, as shown in table 2.4.

Table2.4

Constitutive parameters of SiC particles

σ_f^p/MPa	e_f^p	$e_{\max}^{\mathrm{ck}}$	p
2000	0.2	0.2	2

Notes: σ_f^p is the tensile strength; e_f^p is the fracture strain; p and $e_{\max}^{\mathrm{ck}}$ are material parameters used to control shear retention

(3) Interface Cohesion Constitutive Behavior

The cohesion damage model simulates crack initiation and propagation through the cohesion relationship between materials around the interface[56], which avoids the shortcomings of linear elasticity requiring prefabricated cracks and singularity of crack tips in the specimen, and provides a new means to solve the problem of crack propagation. As a result, the traction-separation criterion and the description of the bilinear model are used to characterize the damage behavior of the interface using the cohesion model (CZM). The bilinear cohesion model [57] is depicted in fig. 2.6.

Given the three-dimensional finite element model, D for damage, range of [0, 1], 0 means the unit did not enter a state of damage. When the cohesive force element reaches the critical effective displacement of damage, it begins to enter the damage evolution stage. With the increase of interface separation displacement, the element generates damage. When the damage amount is equal to 1, the microcrack begins to form. As the external load continues to load, the microcracks continue to expand along the element boundary and eventually lead to material failure. Its expression is [58]:

$$D = \frac{\delta_m^f \left(\delta_m^{\max} - \delta_m^0\right)}{\delta_m^{\max}\left(\delta_m^f - \delta_m^0\right)} \tag{29}$$

Where $\delta_m^{\max}$ is the normal displacement of complete damage; δ_m^f is the temporary crack opening displacement of interface damage; δ_m^0 is the initial displacement normal displacement.

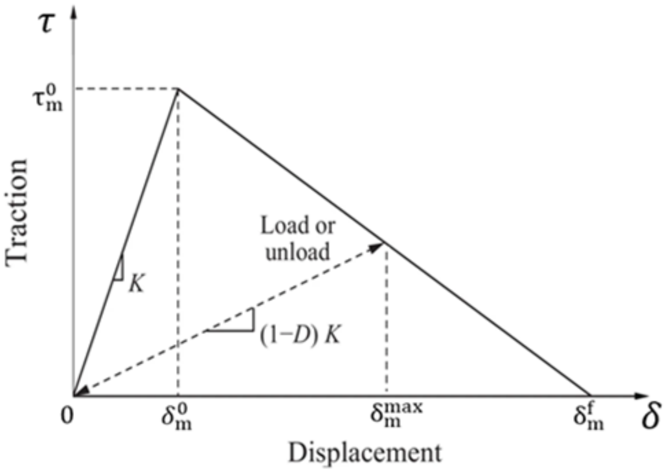

Fig. 2.6. Bilinear cohesive zone model.

Notes: $\delta_m^{\max}$ is the maximum value of the effective displacement; δ_m^f is the effective displacement at complete failure; δ_m^0 is the effective displacement at the initiation of damage; τ_m^0 is the maximum separation stress.

The starting criterion of the cohesive force unit selected in this paper is the maximum nominal stress criterion, assuming that the ratio of nominal stress to maximum stress in the normal direction or any shear direction of the interface is 1, and the interface damage starts. The interface damage expression is:

$$\max\left\{\frac{< t_n >}{t_n^0}, \frac{t_t}{t_t^0}\right\} = 1 \tag{30}$$

Where, t_n^0 and t_t^0 are the critical values of pure tension and pure shear, respectively.

According to reference [23], the constitutive model parameters of the interface between particles and matrix of SiCp/AZ91D composites were obtained as shown in table 2.5.

Table 2.5

Constitutive model parameters of SiC$_p$/AZ91D particle interface

t_n	t_t	δ^{max}	δ^{f}
400MPa	400MPa	0.00015	0.00005

Notes:t_n is the interface normal nominal stress; t_t is the interfacial tangential nominal stress;δ_max is the destruction displacement;δ_f is the material's complete failure separation.

2.2.3 Mesh size, loading, and boundary conditions

The model size is 50 μm × 50 μm × 50 μm, and the global size of the grid is 0.001. The model of SiC original shape particles with a particle size of 10 μm and volume fraction of 15% has 888958 cells and 163993 nodes. There are 28778 COH3D6 (four-node 3D bonded cells) for the interface cells, 136796 and 723384 C3D4 (four-node linear tetrahedral cells) for the particle model and AZ91D matrix model, respectively. M. Galli [59] discussed four other sets of boundary conditions (static uniform, motion uniform, and two mixed static motion uniform) in the uniaxial response of materials with random microstructures. Since this paper is a model with large deformation and large fracture, periodic boundary conditions are no longer applicable. The upper end of the model is applied with -5μm compressive displacement load, the lower end is wholly fixed constraint, the load application time is 15 μs, and the lateral side of the specimen is free boundary conditions. fig. 2.7 (a) shows the meshes of the AZ91D matrix, fig. 2.7 (b) shows the meshes of particles, the yellow arrow above fig. 2.7 (c) shows the loading direction of compressive displacement load, and the arrow below shows the wholly fixed constraint.

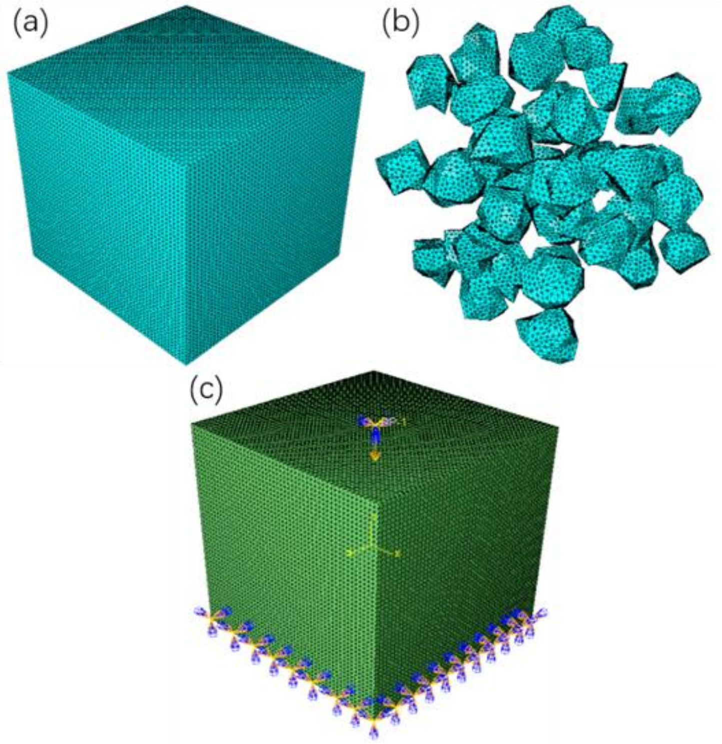

(a) AZ91D matrix meshing (b) SiC particles meshing

(c) Compression loading direction and constraint conditions

Fig. 2.7. Meshing, load imposition, and constraint conditions of SiC$_p$/AZ91D model.

2.2.4 Calculation method of stress and strain values

To obtain the material properties of SiC/AZ9ID magnesium matrix composites under uniaxial compression in the numerical simulation method, (31) and (32) are required to obtain the stress and strain values of the composites at different load steps.

$$\sigma_i = \frac{\sum_k^{Ne} \sigma_k V_k}{V} \tag{31}$$

$$\varepsilon_i = \frac{\sum_k^{Ne} \varepsilon_k V_k}{V} \tag{32}$$

where σ_i and ε_i are the stress and strain values of the composite material at the ith load step, respectively. For the mean calculation, V represents the total cell volume, and σ_k, ε_k, and V_k denote the stress, strain, and volume of the kth cell.

By obtaining the stress and strain values of the microscopic model at different load steps, the stress-strain curve about the SiC/AZ91D composite model as a whole can be obtained and used for further data analysis and comparison.

Summary of this chapter

Based on the real microstructure of SiC_p/AZ91D composites, the dynamic mechanical behavior of the composites is solved by combining advanced image processing techniques and materials science to establish a proven material model, boundary conditions, and loading conditions.

3. 3D FINITE ELEMENT SIMULATION OF SiC/AZ91D COMPOSITES

3.1 Effect of particle volume fractions

To investigate the effect of SiC particle volume fraction on crack initiation and propagation of composites, a composite model with the particle size of 10μm and volume fraction of 5%, 10%, 15%, and 20% was established, as shown in Fig. 3.1. The particles were randomly distributed in the AZ91D matrix.

Fig. 3.2 shows the stress-strain curves of the matrix and SiC/AZ91D composites with different particle volume fractions during compression. From the figure, it can be seen that in the online elastic stage, the stress value of the matrix is 77.306 MPa, and the stress values of the composites with particle volume ratios of 5%, 10%, 15%, and 20% are 209.126 MPa, 221.576 MPa, 238.539 MPa, and 246. 632 MPa, respectively. In the yield stage, the stress value of the matrix is 160.034Mpa, and the stress value of composites with particle volume fraction of 5%, 10%, 15%, and 20% is 241.511 Mpa, 256.366MPa, 265.577 MPa, and 276.273 MPa, respectively.

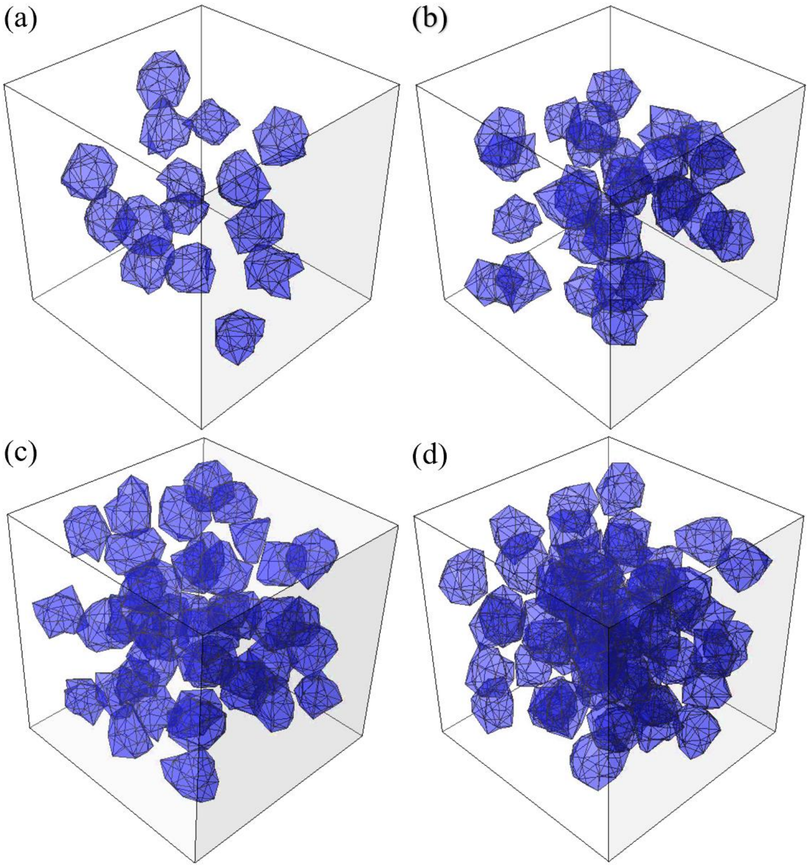

(a) volume fraction 5% (b) volume fraction 10% (c) volume fraction 15% (d) volume fraction 20%

Fig. 3.1. Model diagram of SiC/AZ91D composites with different particle volume fractions.

The stress value of the composites is higher than that of the AZ91D matrix in both the online elastic stage and the yield stage, and the greater the particle volume fraction, the greater the stress value of the composites. In the yield phase, SiC particles bear part of the load transferred by the AZ91D matrix during the compression process. With the increase of particle volume fraction, more SiC particles bear the load and the load is evenly distributed on the particles. As a result, the composites can bear more stress under the same strain, and the yield strength of the composites increases with the increase of particle volume fraction.

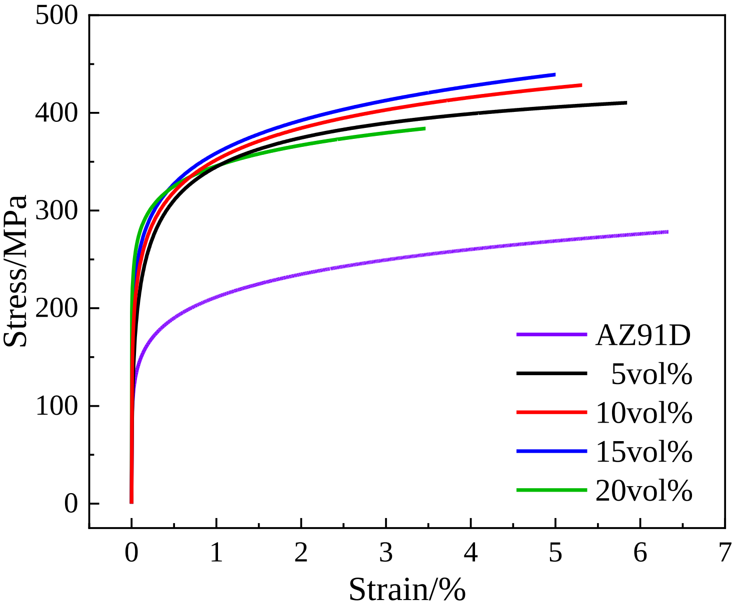

Fig. 3.2. Compression stress-strain curves of the matrix and SiC_p / AZ91D composites with different particle volume fractions.

Fig. 3.3 displays the matrix and SiCp/AZ91D composites' yield strength, compressive strength, and compressibility at various particle volume fractions. The compressive strength increases from 409.529MPa to 440.874MPa, the compressibility drops from 5.838% to 4.993%, and the particle volume fraction rises from 5% to 15%, as shown in fig. 3.3. The compressive strength of the composite reduces from 440.874 MPa to 386.017 MPa, and the compressibility decreases from 4.993% to 3.465%, when the particle volume percent rises from 15% to 20%. The composites' compressive strength gradually diminishes as the compressibility gradually increases.

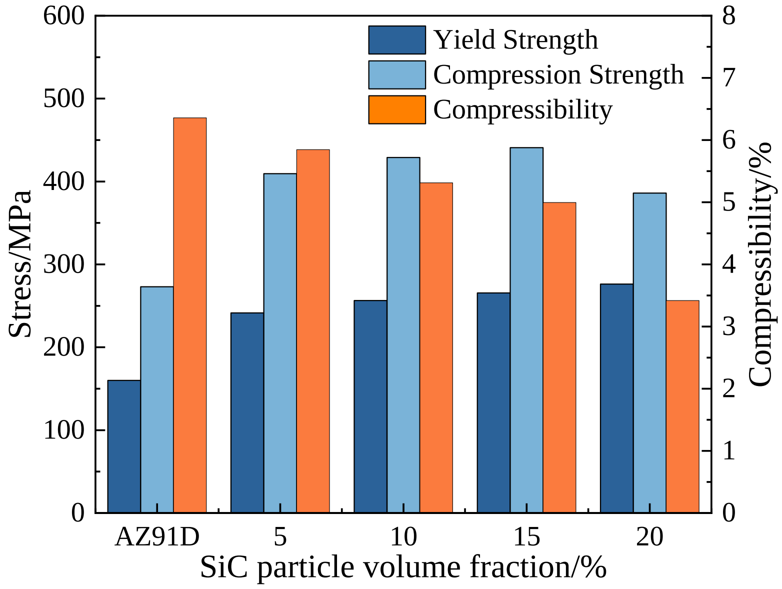

Fig. 3.3. Yield strength, compressive strength, and compressibility of the AZ91D matrix and SiC_p/AZ91D composites with different particle volume fractions during compression.

The compressive strength of the composites first increases and then decreases, and the compressibility gradually decreases. The compressive strength of composites increases as the particle volume fraction increases. The reason is that when the particle volume fraction is low(particle volume fraction ≤15%), the SiC particles bear a portion of the load transferred by the AZ91D during the compression process. As the particle volume fraction increases, more SiC particles bear the load, and the load is evenly distributed on the particles, resulting in a composite that can withstand tremendous stress. When the SiC particle volume fraction is greater (particle volume fraction > 15%), there are numerous small spaces between the particles. The angle between the particles and the matrix caused by the stress concentration is too great, preventing the matrix from effectively responding to the grain and causing the particles to bear the stress of the angle of ultimate strength more impressively than the substrates. The compressive strength of the composites decreases as particle volume rises. As for the decline of the compressibility, this is because the particle-matrix interface area grows, which strengthens the grain boundary and prevents the composites' dislocations from moving during compression, reducing the plasticity of the material.

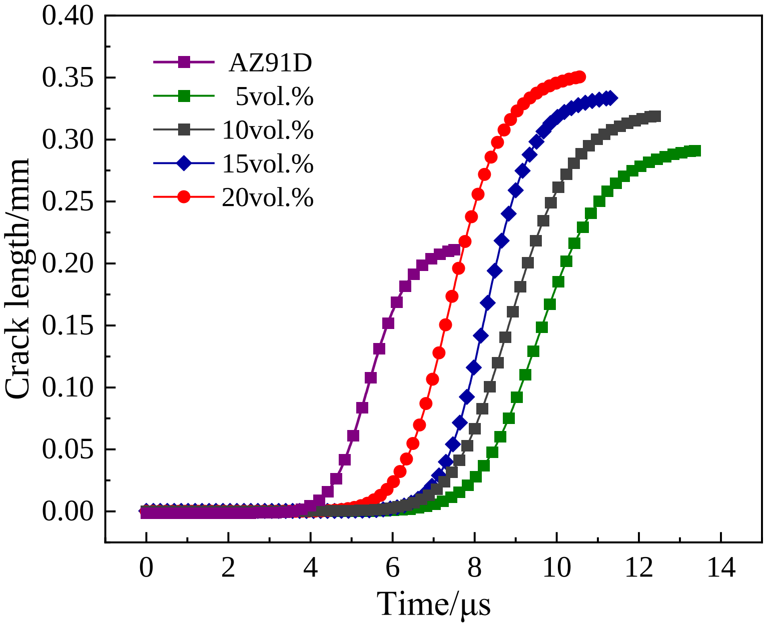

Fig. 3.4. Crack length curves with time for AZ91D matrix and SiC_p/AZ91D composites with different particle volume fractions.

Fig. 3.4 shows the crack length curves of AZ91D matrix and composites with 5%, 10%, 15%, and 20% particle volume fractions as a function of time. As can be seen from fig. 3.4, crack propagation in composites with four-particle volume fractions causes overall instability and rapid fracture of composites to a certain extent. The crack initiation time of composites with equivalent particle sizes of 5, 10, 15, and 20 μm are 7.2 μs, 6.3 μs, 5.7 μs, 4.8μs and the fracture time are 12.3 μs, 11.3 μs, 10.7 μs, 9.9 μs after loading. Compared with the AZ91D matrix, both the crack initiation and fracture times of the composites are delayed.

As a result, it can be seen that adding particles can slow the initiation and propagation process of cracks in composites, whereas increasing the particle volume fraction will speed up the process. The reason is that the addition of particles will significantly increase the dislocation density in the deformation process of the composite material, the composites can bear more loads than the AZ91D matrix, and the composites are not easy to produce microcracks, so the crack germination and fracture time are increasingly delayed. When the particle volume fraction is low (particle volume fraction ≤15%), the reinforced particles are evenly distributed in the matrix and bear a greater share of the load, making it more difficult for the stress value to exceed the matrix's compressive strength value. When the SiC particle volume fraction is high (particle volume fraction >15%), the stress value quickly reaches and exceeds the compressive strength value of the matrix, and the secondary cracks quickly join, penetrate, and converge into primary cracks, causing the composites to fracture.

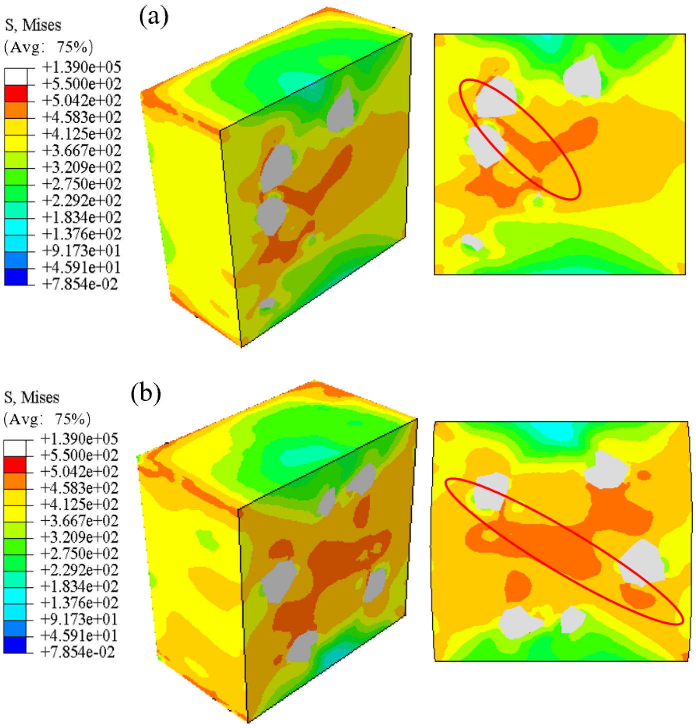

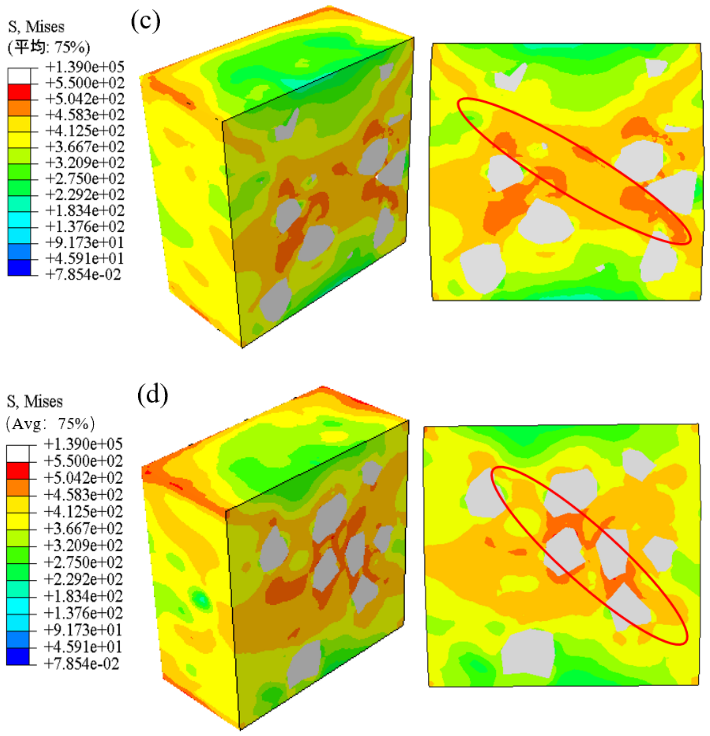

(a) volume fraction 5% germination condition (b) volume fraction 10% germination condition

(c) volume fraction 15% germination condition (d) volume fraction 20% germination condition

Fig. 3.5. Germination of SiC_p/AZ91D composites with different particle volume fractions after loading.

Fig. 3.5 shows the crack germination at 7.2 μs, 6.9 μs, 6.3 μs, and 5.3 μs after loading for composites with different particle volume fractions. As seen in fig. 3.5, it can be seen that there is a significant stress concentration zone at 45 degrees to the compression direction, and cracks also appear in the composite with four-particle volume fractions. During the compression of composites, the stress tends to concentrate on the sharp corners of the particle edges. The primary cause of this phenomenon is the ease with which the stress can concentrate at the acute angle of the particle edge during the compression of the composites. When the stress at the interface between the SiC particles and the matrix approaches the matrix's maximal strength, microcracks will start to form in the material. The crack initiation times of the four composites with various particle volume fractions during loading show that decreasing the particle volume fraction will reduce the composites' crack initiation periods and speed up the fracture propagation process. Microcracks will begin to form in the matrix when the stress at the interface between the SiC particles and the matrix approaches the matrix's maximum strength.

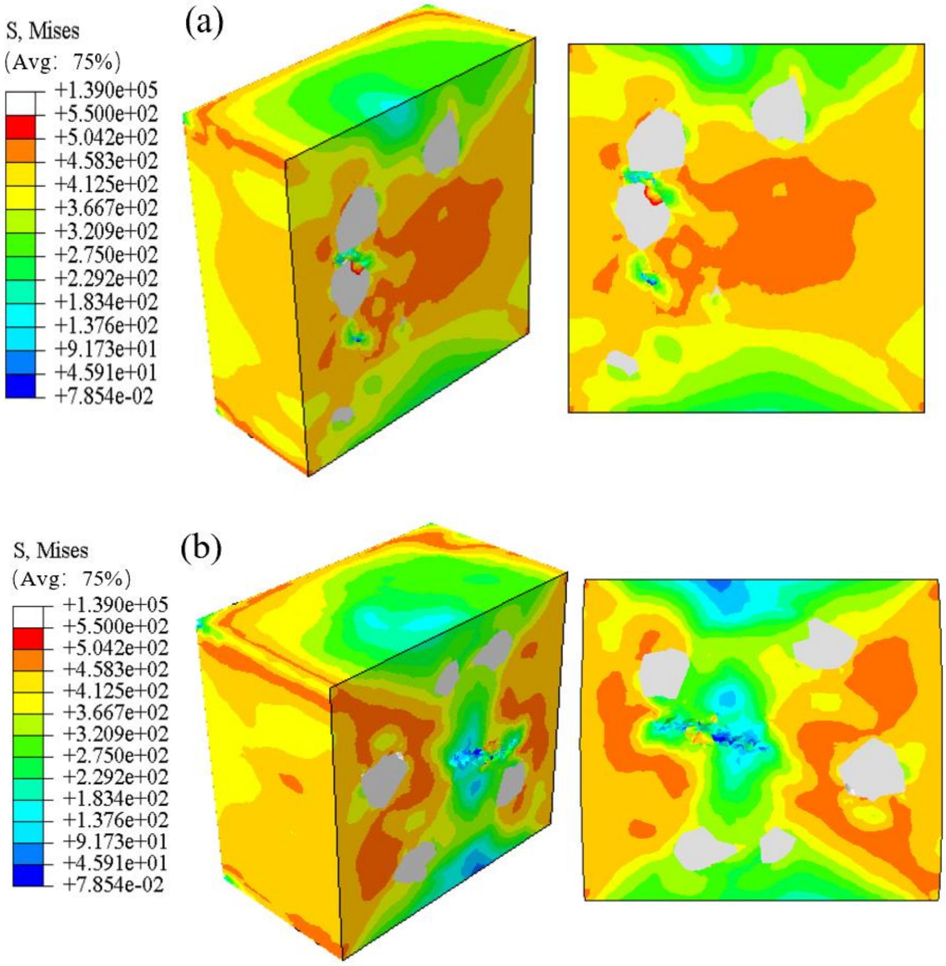

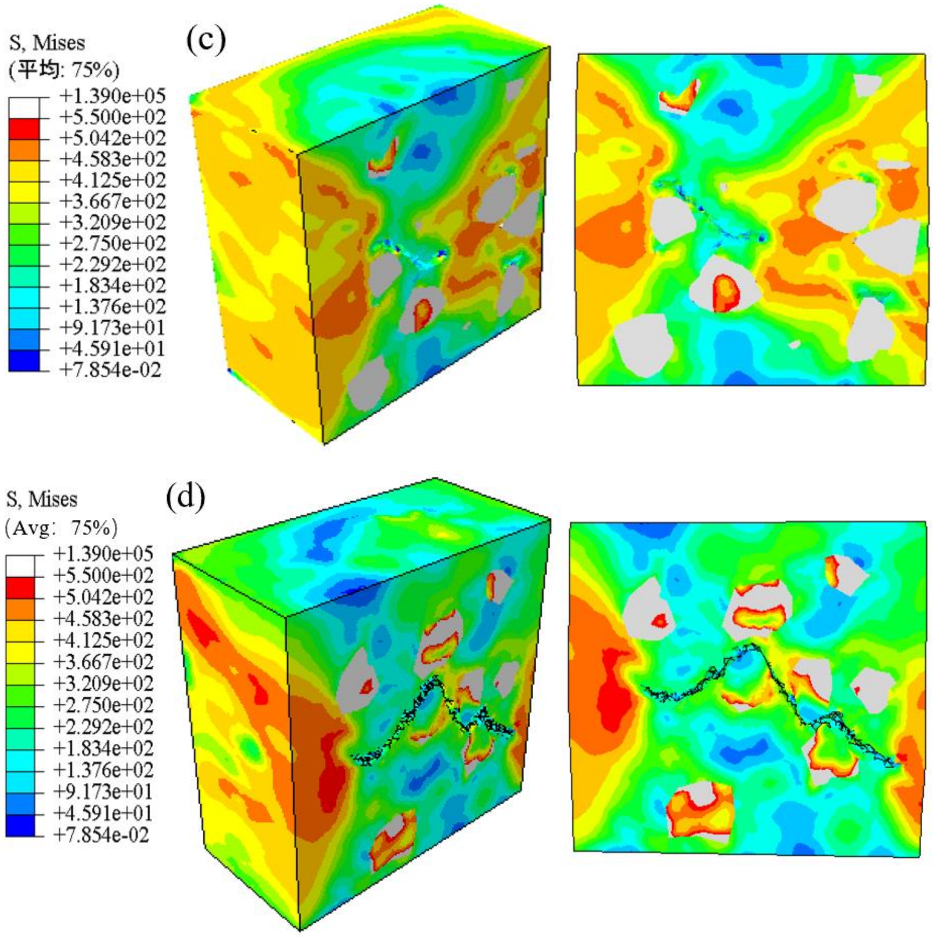

(a) Crack growth with a volume fraction of 5% (b) crack growth with a volume fraction of 10%

(c) Crack growth with a volume fraction of 15% (d) crack growth with a volume fraction of 20%

Fig. 3.6. Crack propagation of SiC_p/AZ91D composites with different particle volume fractions after loading.

Fig. 3.6 shows the crack propagation of composites with particle volume fractions 5%, 10%, 15%, and 20% at the 9th μs after loading. As seen in fig. 3.6, the matrix develops microcracks as a result of a significant stress concentration at the point where the sharp angle of the particles meets the matrix. The microcracks are connected to form the main crack. The path of greatest shear stress is where the crack spreads. Due to the great strength of SiC particles, the driving force of crack propagation can only move along the edges of

SiC particles because it is unable to destroy them. The microcracks converged into the main crack when the composite with a particle volume percentage of 5% was loaded at 12.9 μs. The microcracks converged into the main crack when the composites with a particle volume percentage of 10% were loaded at 12.3 μs. The primary crack and secondary fractures that resulted in a material fracture were generated when the composites with a 15% particle volume fraction were loaded at 11.7 μs. The primary crack and secondary crack linked when the composites with a 20% particle volume fraction were loaded at 10.2 μs. Accordingly, the three different types of composite crack extension are different; the low volume fraction of microcracks in composites to assemble the main crack, crack is not secondary, and the high volume fraction of microcracks in composites not only to assemble the main crack but crack is also accompanied by secondary.

3.2 Effect of equivalent particle sizes

As shown in fig. 3.7, the composite model with the particle volume fraction of 15% and the particle equivalent particle size of 5, 10, 15, and 20μm are established to explore the effect of the particle equivalent particle size on the crack initiation and propagation of the composite.

Fig. 3.7 shows the stress-strain curves of the AZ91D matrix and composites with different equivalent particle sizes during compression. As can be seen from the figure, in the linear elastic stage, the stress value of the AZ91D matrix is 77.306 MPa, and the stress values of the composites with equivalent particle sizes of 5, 10, 15, and 20 μm are 249.837 MPa, 238.539 MPa, 220.348 MPa, and 208.568 MPa, respectively.

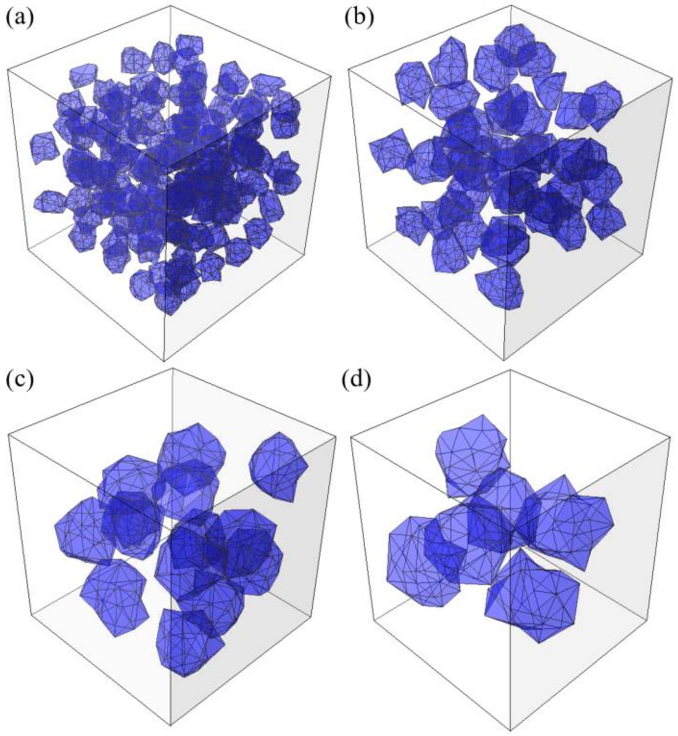

(a) equivalent particle size 5μm model (b) equivalent particle size 10μm model

(c) equivalent particle size 15μm model (d) equivalent particle size 20μm model

Fig. 3.7. Model diagram of SiC$_p$/AZ91D composites with different particle sizes.

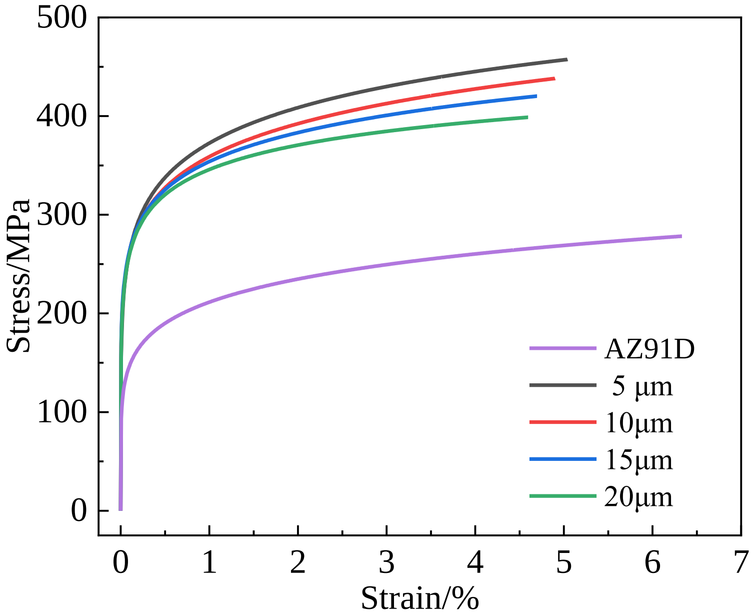

Fig. 3.7. Stress-strain curves of the AZ91D matrix and SiC$_p$/AZ91D composites with different equivalent particle sizes during compression.

In the yield stage, the matrix stress is 160.034 MPa, and the yield stresses of the composites with equivalent particle sizes of 5, 10, 15, and 20 μm were 279.839 MPa, 265.577 MPa, 259.892 MPa, and 250.722 MPa, respectively. The stress values of the composites were higher than those of the AZ91D matrix in both the linear elastic and yielding stages. And the smaller the equivalent particle size, the higher the stress values of the composites. The reason is that the elastic modulus of the particles and the matrix are different after the applied load, resulting in different deformations of the different materials. To maintain the continuity of deformation between the crystals, a certain degree of dislocation is generated. The addition of particles will significantly increase the dislocation density during the deformation of the composite, and the composite can withstand more load than the matrix. As the equivalent particle size decreases, the more particles per unit volume, the easier the dislocations will accumulate in the matrix. And the more obvious the reinforcement of dislocations will be, which leads to the greater the stress value of the composites.

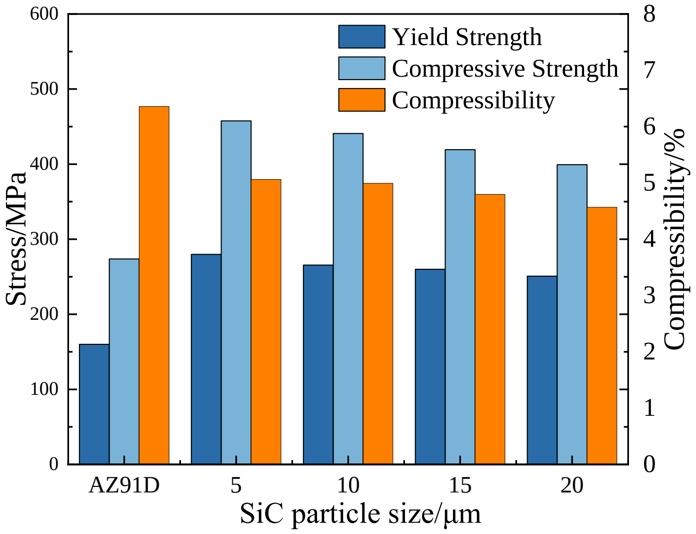

Fig. 3.8. Yield strength, compressive strength, and compressibility of the AZ91D matrix and SiC_p/AZ91D composites with different particle sizes during compression.

Fig. 3.8 shows the bar graphs of yield strength, compressive strength, and compressibility of the matrix and SiC_p/AZ91D composites with different equivalent particle sizes during compression. As can be seen from fig. 3.8, the particle size also has a certain impact on the compressive strength and compressibility of the composites. The compressive strength of the matrix is 273.626 MPa, and the compression rate is 6.358%. The compressive strengths of the composites with equivalent particle sizes of 5, 10, 15, and 20 μm are 457.66 MPa, 440.874 MPa, 419.334 MPa, and 399.278 MPa, respectively, and the compression rates are 5.061%, 4.993%, 4.796%, and 4.569%, respectively. Compared with the matrix alloy, the compressive strength of the composite is greatly increased, while the compression rate is decreased. In addition, the properties of SiC_p/AZ91D composites with different equivalent particle sizes are not the same. The reason is that when the volume fraction is fixed, the smaller the reinforced particle size is; the higher the dislocation density will be during deformation, the better the strengthening effect will be, and the stronger the ability of the composite to bear the load will be. Therefore, the smaller the equivalent particle size, the higher the compressive strength and the better the plasticity of the composite.

The variation curve of crack length with time after loading for the matrix and composites with different particle sizes is shown in fig. 3.9. From the figure, the crack budding and fracture times of the AZ91D matrix were 4.3 μs and 7.2 μs, and the crack length shows an increasing trend with the decrease in particle size. The crack initiation time of composites with equivalent particle sizes of 5, 10, 15, and 20 μm are 7.2 μs, 6.3 μs, 5.7 μs, 4.8 μs and the fracture time are 12.3 μs, 11.3 μs, 10.7 μs, 9.9 μs after loading, respectively. Compared with the AZ91D matrix, both the crack initiation and fracture times of the composites are longer. This indicates that particle incorporation can delay the crack germination and propagation of the composites and the smaller the equivalent particle size is, the more conducive to crack initiation and propagation inhibition. The root cause of composite fracture is stress concentration at the junction of the particle's sharp Angle and matrix, where the stress quickly reaches or even exceeds the ultimate strength of the matrix, and the crack is induced by matrix damage.

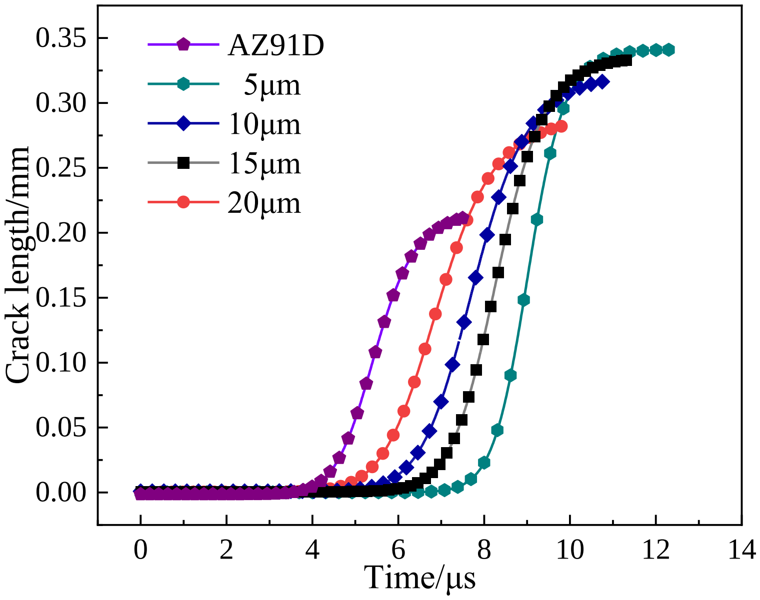

Fig. 3.9. Crack length curves with time for AZ91D matrix and SiC_p/AZ91D composites with different equivalent particle sizes.

It is necessary to circumvent particles during crack propagation. When the particle volume fraction is fixed, the smaller the particle size, the more particles in the unit volume, the particles are more evenly distributed in the matrix to share part of the load, and the matrix stress is difficult to reach its ultimate compressive strength value, so the crack is not easy to initiate. Even if the crack is initiated, its expansion process needs to circumvent more particles and the expansion path is tortuous. Therefore, compared with the matrix, the crack of composites is not easy to germinate and propagate, and the smaller the particle size is, the less easy the crack germination and propagation is, indicating that the smaller the particle size is, the more conducive to inhibiting the crack initiation and propagation fracture of composites.

Fig. 3.10 shows the crack germination at 7.2 μs, 6.3 μs, 5.7 μs and 4.8 μs after loading for composites with different particle sizes. As shown in fig. 3.10 (a), the crack bud of composites with a particle size of 5μm occurred at the 7.2 μs after the load was applied.

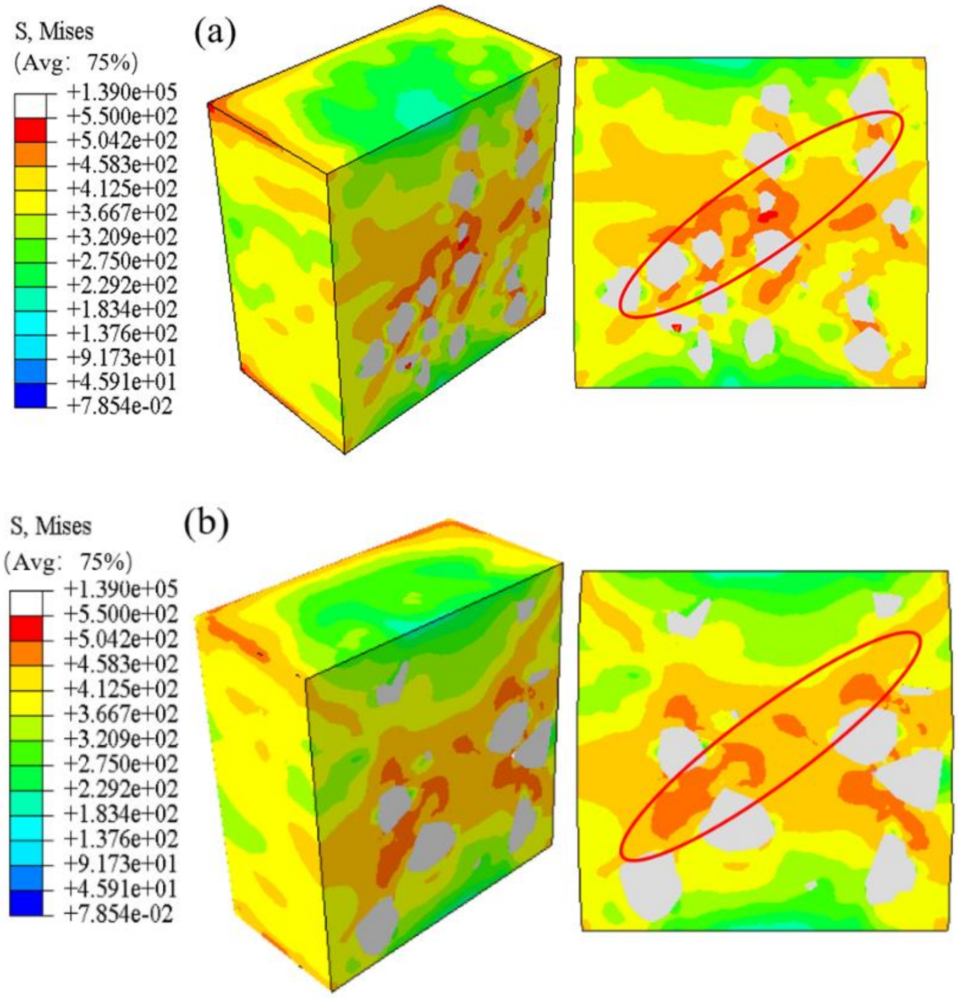

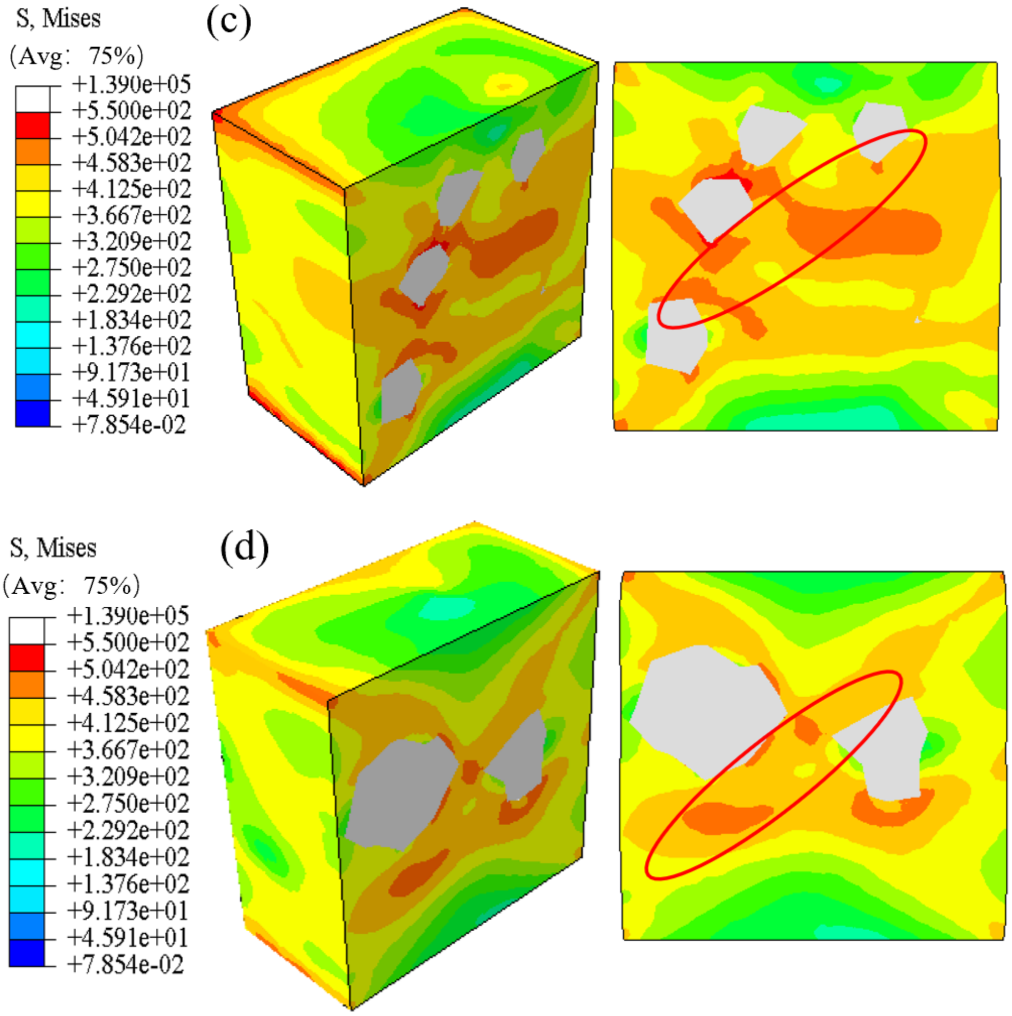

(a)Size 5μm germination condition (b) Size 10μm germination condition

(c) Size 15μm germination condition (d) Size 20μm germination condition

Fig. 3.10. Crack germination of SiC_p/AZ91D composites with different particle sizes after loading.

As shown in fig. 3.10 (b), the crack bud of composites with a particle size of 10 μm occurred at the 6.3μs after the load was applied. As shown in fig. 3.10 (c), the crack bud of the composite with a particle size of 15 μm occurred at the 5.7 μs after the load was applied. As shown in fig. 3.10 (d), the crack bud of the composites with a particle size of 20 μm occurred at 4.8 μs after the load was applied. In the figure, there are obvious stress concentration zones at the places marked by the red ellipse box and 45 degrees from the compression direction. The crack buds mainly appear at the sharp corners of grain cusps, and a few appear in the matrix between particles. The reason for this phenomenon is that during the compression process, plastic deformation occurs in the composites along the direction of maximum shear stress, and the stress is easy to accumulate at the sharp angle of the particle edge.

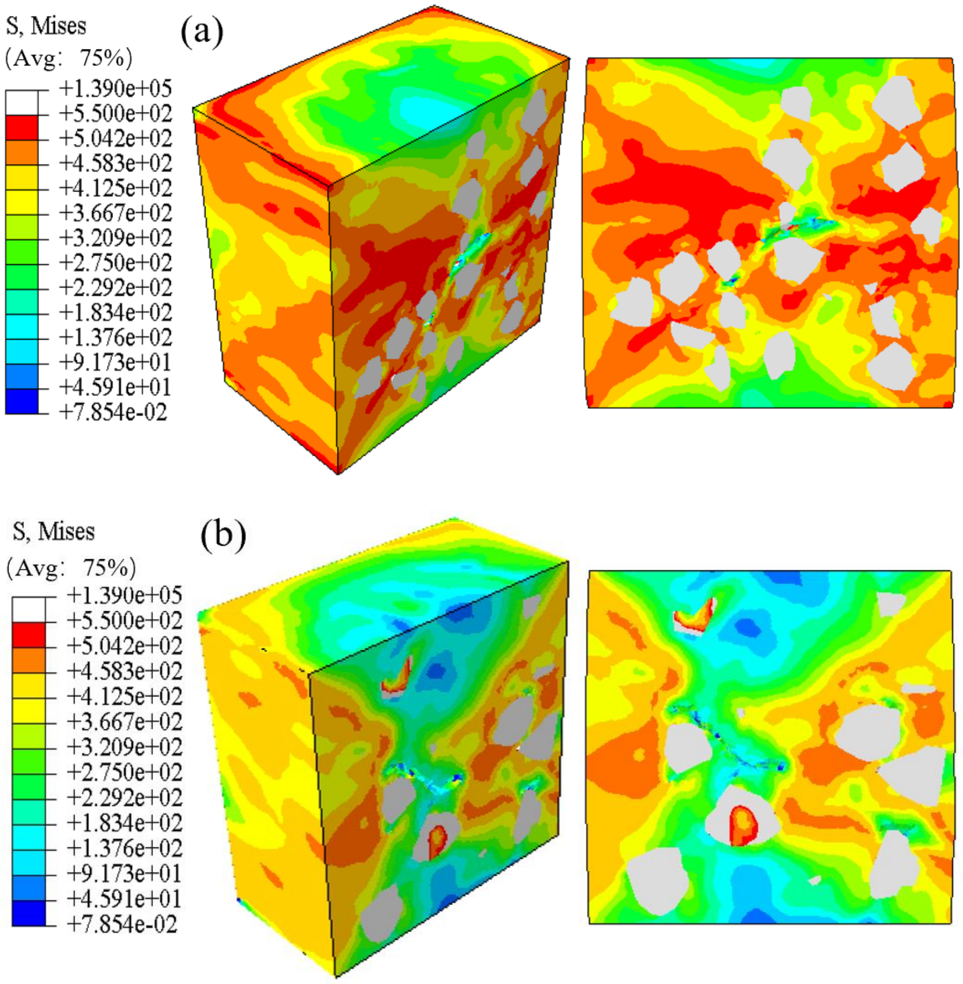

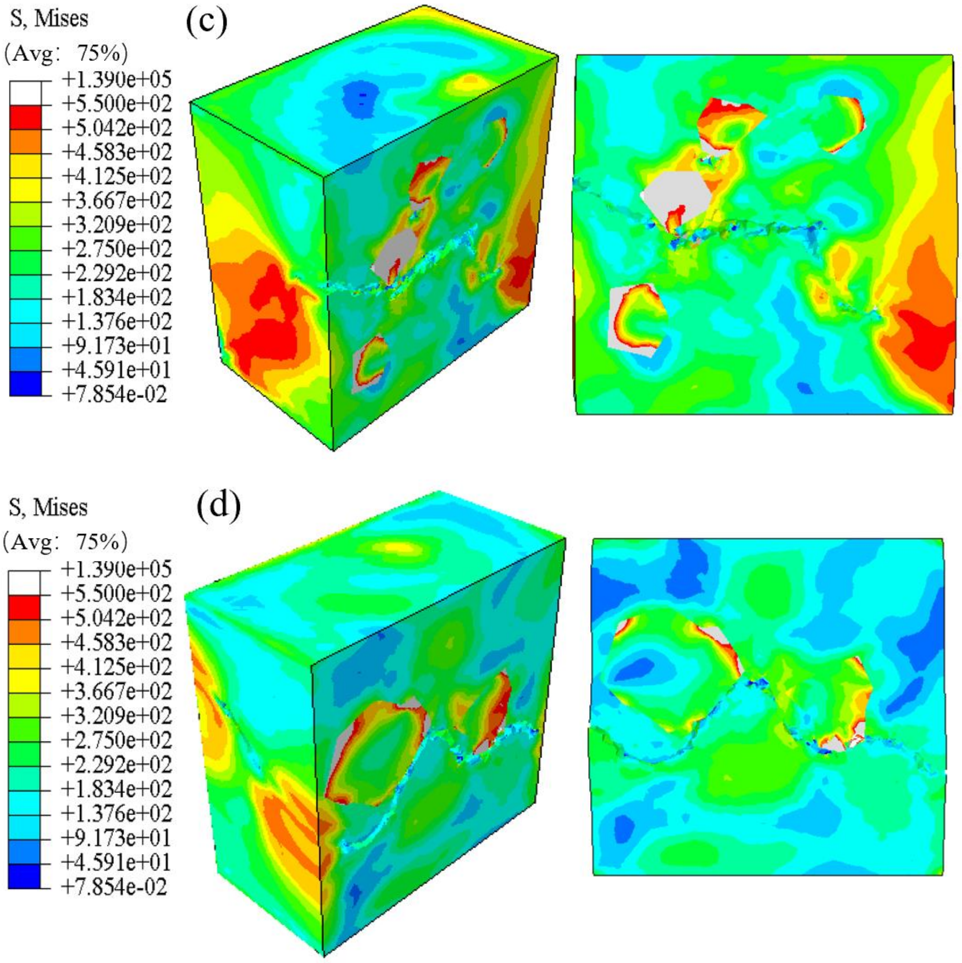

(a)Particle size 5μm expansion (b) Particle size 10μm expansion

(c) Particle size 15μm expansion(d) Particle size 20μm expansion

Fig. 3.11. Crack propagation of SiC/AZ91D composites with different particle sizes after loading.

Fig. 3.11 shows the crack propagation of composites with equivalent particle sizes of 5, 10, 15, and 20 μm at the 9th μs after loading. It can be seen from the figure that the larger the equivalent particle size is, the more serious the crack propagation degree is. This is because each particle is carrying more and more load. The microcrack is initiated at the junction of the particle and the matrix and then expands around the boundary or sharp corner of the SiC particle along the direction of maximum shear stress, forming the main crack.

During the loading process, the stress is more likely to be concentrated at the sharp Angle of the particle with a large equivalent particle size. Because the strength of SiC particles is much higher than the ultimate strength of the matrix, micro-cracks are generated in the matrix in contact with the particles. The crack propagates to the boundary or sharp corner of the SiC particle and deflects to form the main crack.

3.3 Effect of particle shapes

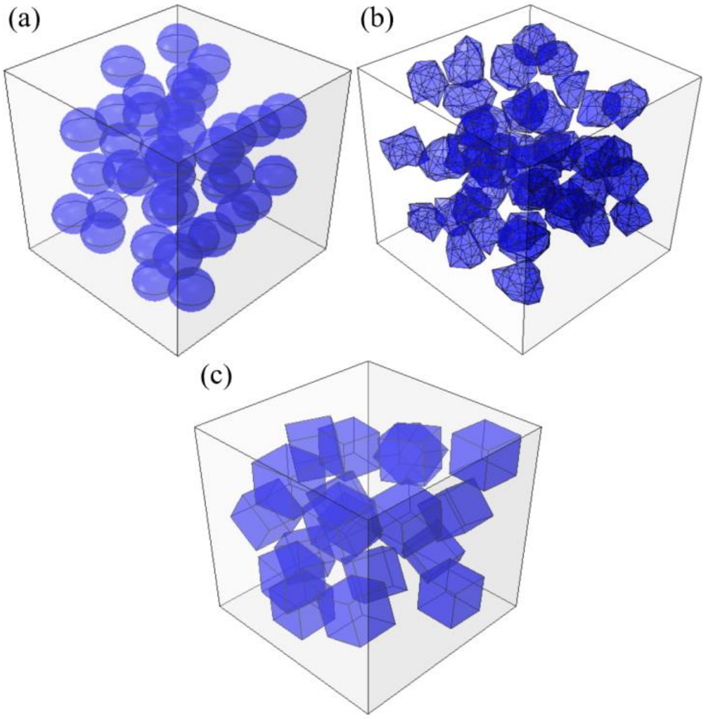

(a)Circular SiC particle (b)Original shape SiC particle (c)Square SiC particle

Fig. 3.12. 3D Model diagrams of SiC/AZ91D magnesium matrix composites with different particle shapes.

As shown in fig. 3.12, 3D composite models with circular, primitive, and square particle shapes were established to investigate the effect of different shapes of SiC particles on the crack sprouting and expansion of the composite.

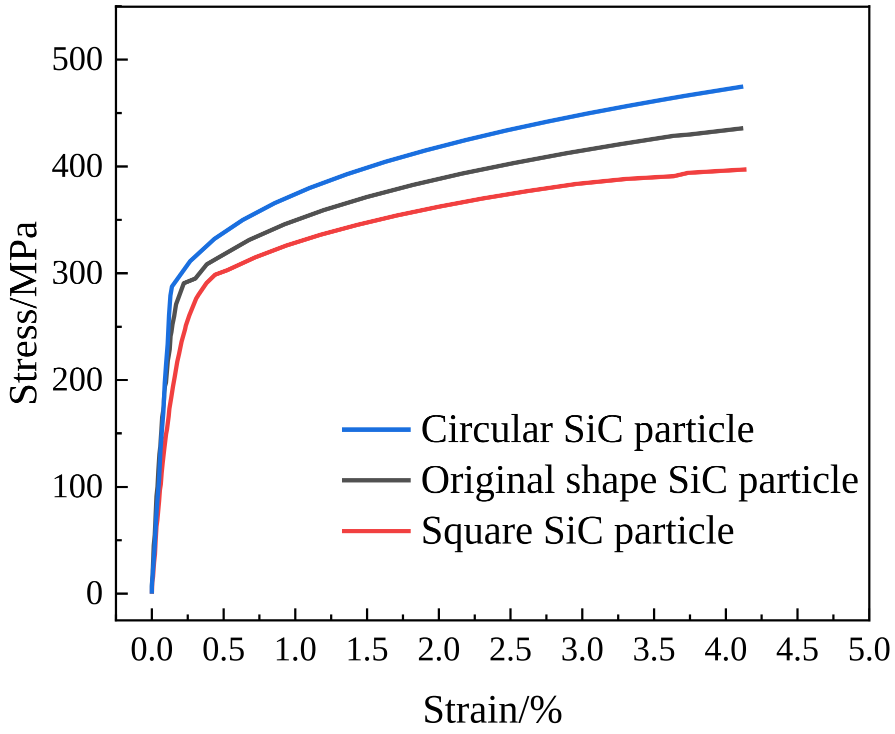

Fig. 3.13. Stress-strain curves of SiC/AZ91D magnesium matrix composites with different shapes of particles during compression.

The compressive stress-strain curves of the composites with different particle shapes are shown in fig. 3.13. It can be seen that the stress values of the composites are 252.196 MPa, 238.539 MPa, and 202.322 MPa for round, pristine and square particles, respectively, in the linear elastic phase, and 279.747 MPa, 265.577 MPa, and 224.522 MPa for round, pristine and square particles, respectively, in the yield phase. The stress values of the composites increased with the increase of particle roundness in both the inline elastic stage and the yielding stage because the round particles can distribute the load transferred to the particles more uniformly at the junction of the particle-matrix interface in the load transfer, which reduces the stress concentration at the particle-matrix interface.

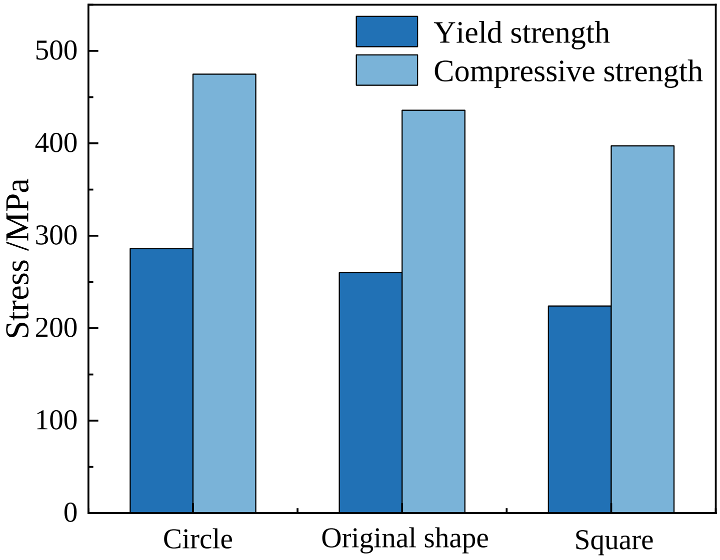

Fig. 3.14. Histogram of yield strength and compressive strength of SiC/AZ91D magnesium matrix composites with different shapes of particles during compression.

As can be seen from fig. 3.14, the particle shape has a certain influence on the yield strength and compressive strength of the material, and the compressive strength of the composite material with round, original shape, and square particles are 474.853 MPa, 440.874 MPa, and 397.211 MPa, respectively. The yield strength and compressive strength of the composite material are gradually decreasing as the particle shape becomes sharper because after the particles enter the yielding stage, the stress concentration caused by particles with sharp corners is more likely to damage the matrix, with square particles causing the most serious damage to the matrix.

Fig. 3.15 shows the crack length curves with time after loading for the composites with round, pristine shape, and square particles. It can be seen from the figure that with the increase of particle roundness, the crack length shows an increasing trend, and the crack budding and fracture times of circular, primitive shape and square particle composites are 8.3 μs, 6.3 μs, 5.6 μs and 12.2 μs, 11.3 μs, 9.6 μs after loading, respectively.

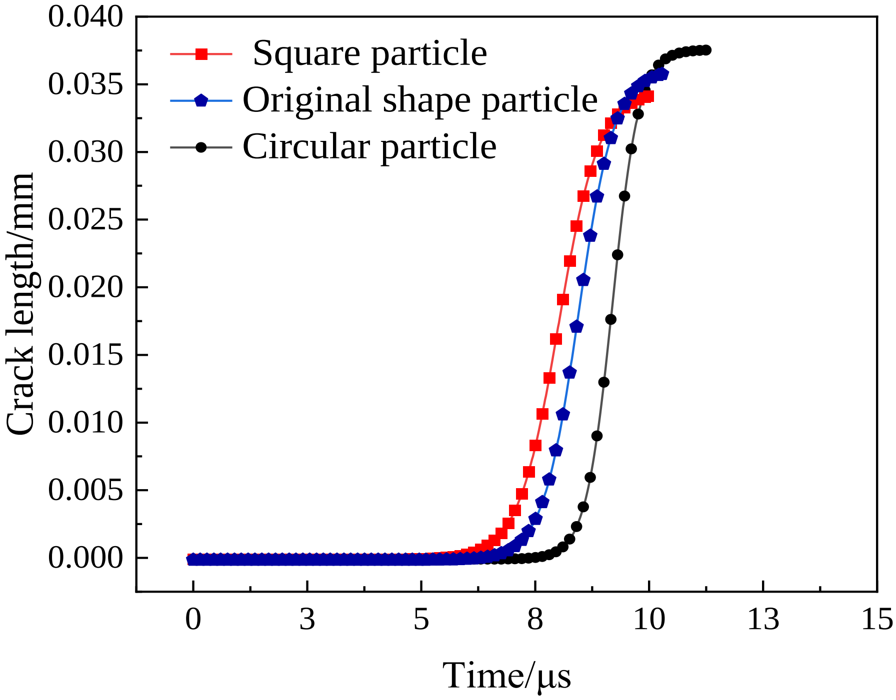

Fig. 3.15. Curves of the crack length of SiC/AZ91D magnesium matrix composites with different particle shapes over time.

Fracture is the second, and the composites with square particles fracture the fastest. Round particles have rounded borders, and the stress concentration is not easy to appear at the junction of particles and matrix, and the root cause of fracture is that the stress that the particles can bear is much higher than the ultimate strength that the matrix can bear. The boundary of the original shape of the particles is sharper, and the junction of the sharp corner of the particles and the matrix is prone to stress concentration, and the stress there quickly reaches or even exceeds the ultimate strength of the matrix, resulting in microcracks easily generated in the matrix there, and the crack expansion rate is larger, and the crack expansion process does not need to bypass the merging of particles connected to the main crack, so the crack expansion length is shorter.

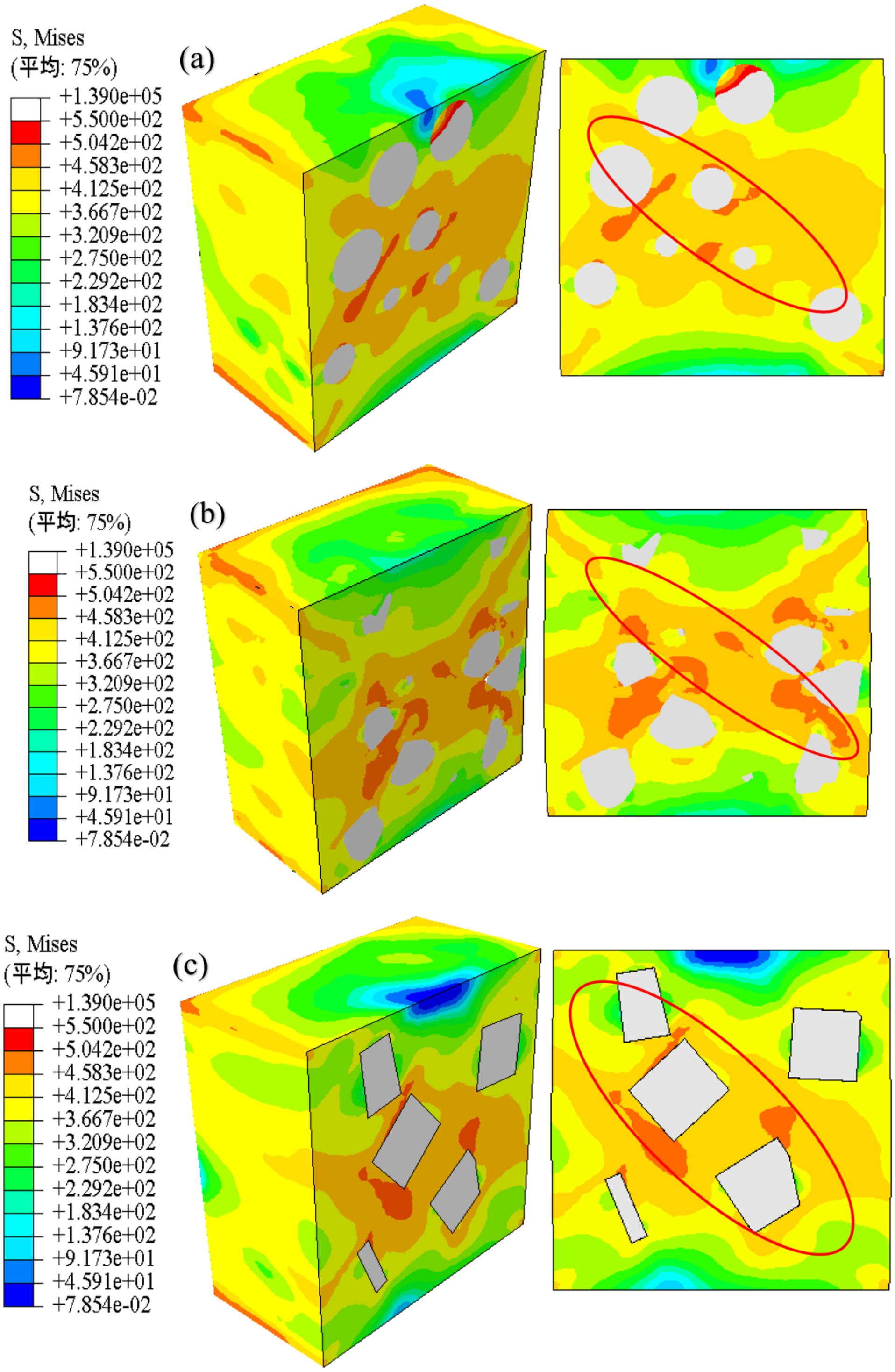

(a) Germination of circular particles at 8.3 μs (b) Germination of the original shape particles at 6.3 μs (c) Germination of square particles at 5.6μs

Fig. 3.16. Crack germination of SiC/AZ91D magnesium matrix composites with particles of different shapes after loading.

Fig. 3.16 (a), fig. 3.16 (b), and fig. 3.16 (c) show the crack sprouting for the composites with circular, primitive shapes and square particles, respectively. The crack budding of the circular particle composite shown in Fig. 3.16 (a) occurs at the 8.3 μs after load application; the crack budding of the primitive shape particle composite shown in Fig. 3.16 (b) occurs at the 6.3 μs after load application; the crack budding of the square particle composite shown in Fig. 3.16 (c) occurs at the 5.6 μs after load application. it can be seen that the crack budding of the circular particle composite occurs at all In contrast, the square particles and the original shape particles have sharp edges and corners compared with the round particles, and there is a serious stress concentration at the interface between the particles and the matrix, so the crack budding of the composite material mainly occurs at the matrix at the junction with the sharp edges and corners particles, and also in the matrix between the particles.

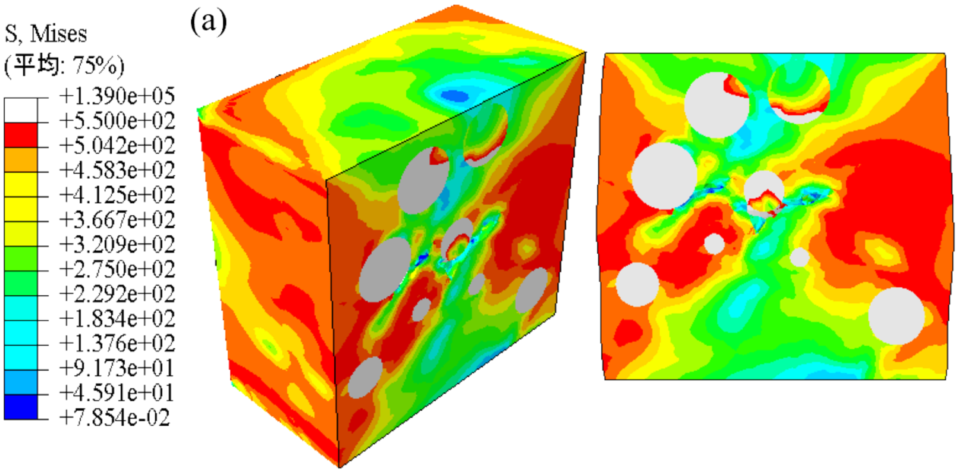

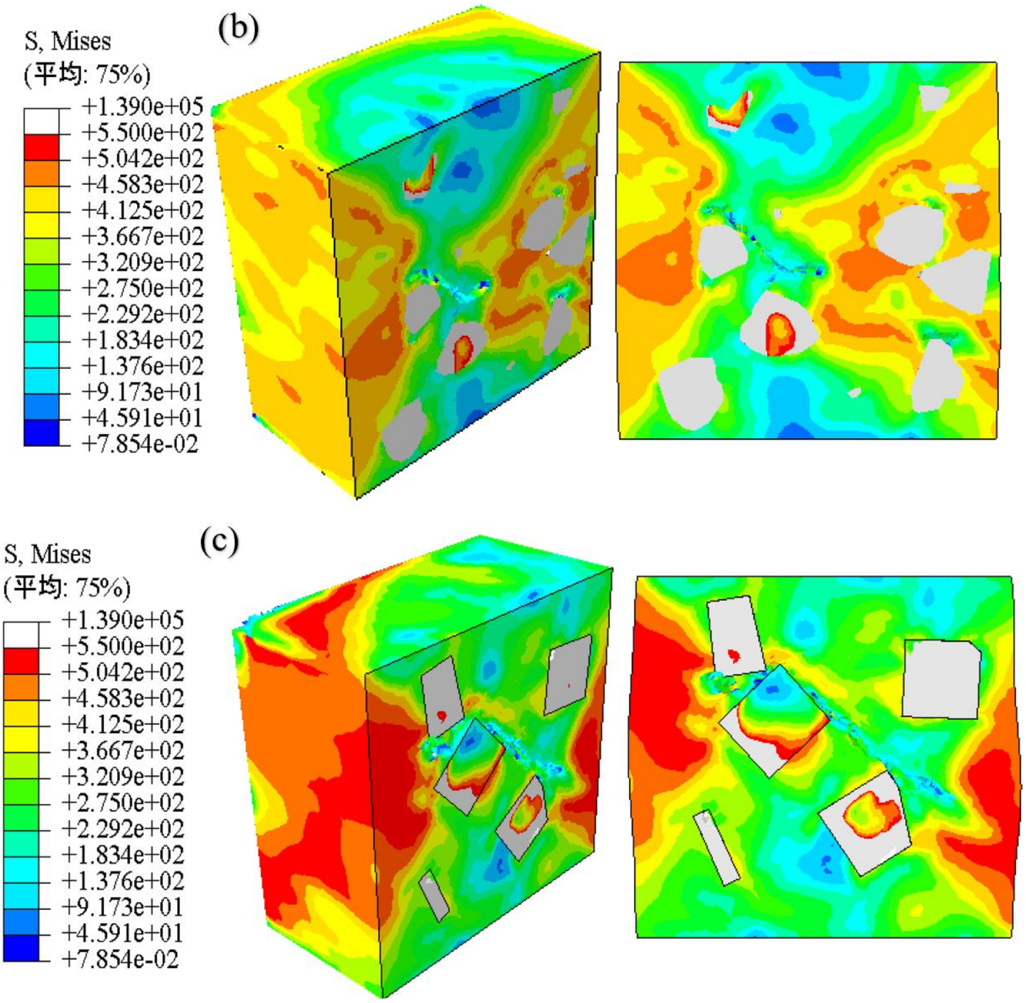

(a) Circular particle expansion (b) Original shape particle expansion (c) Square particle expansion

Fig. 3.17. Crack growth of SiC/AZ91D magnesium matrix composites with particles of different shapes after loading.

Fig. 3.17 (a), fig. 3.17 (b), and fig. 3.17 (c) show the crack expansion at 9 μs after loading the composite with round particles, original-shape particles, and square particles. As can be seen from the figures, when the particles are round, there is no obvious stress concentration at the junction between the boundary of round particles and the matrix, and most of the microcracks emerge from the matrix damage, and the microcracks caused by the matrix damage are interconnected and penetrated to form primary cracks in the matrix, but there are no secondary cracks in the matrix near most of the round SiC particles; when the particles are square or primitive shape, the microcracks first emerge at the junction between the particles and the matrix, and then along the relative When the particles are square or primitive in shape, the microcracks first emerge at the junction of the particles and the matrix, and then expand around the boundary or sharp corner of the SiC particles along about 45° concerning the loading direction, forming the primary crack. Since the stresses carried by the particles are much higher than the ultimate strength of the matrix, the cracks are deflected at the boundary or sharp corner of the SiC particles and expand in the direction of the maximum tangential stress of the matrix; the stress concentration at the junction of the sharp corner of the particles and the matrix accelerates the formation of primary cracks in the composite on the one hand, and promotes the emergence and connection of secondary cracks on the other hand; the presence of round particles plays an obvious role in inhibiting the crack expansion in the composite. The presence of round particles has a significant inhibitory effect on the crack expansion in the composite, while the square shape and the original shape of particles with sharp corners play a certain role in promoting the crack expansion in the composite.

3.4 Matrix damage of SiC/AZ91D composites at the complete fracture

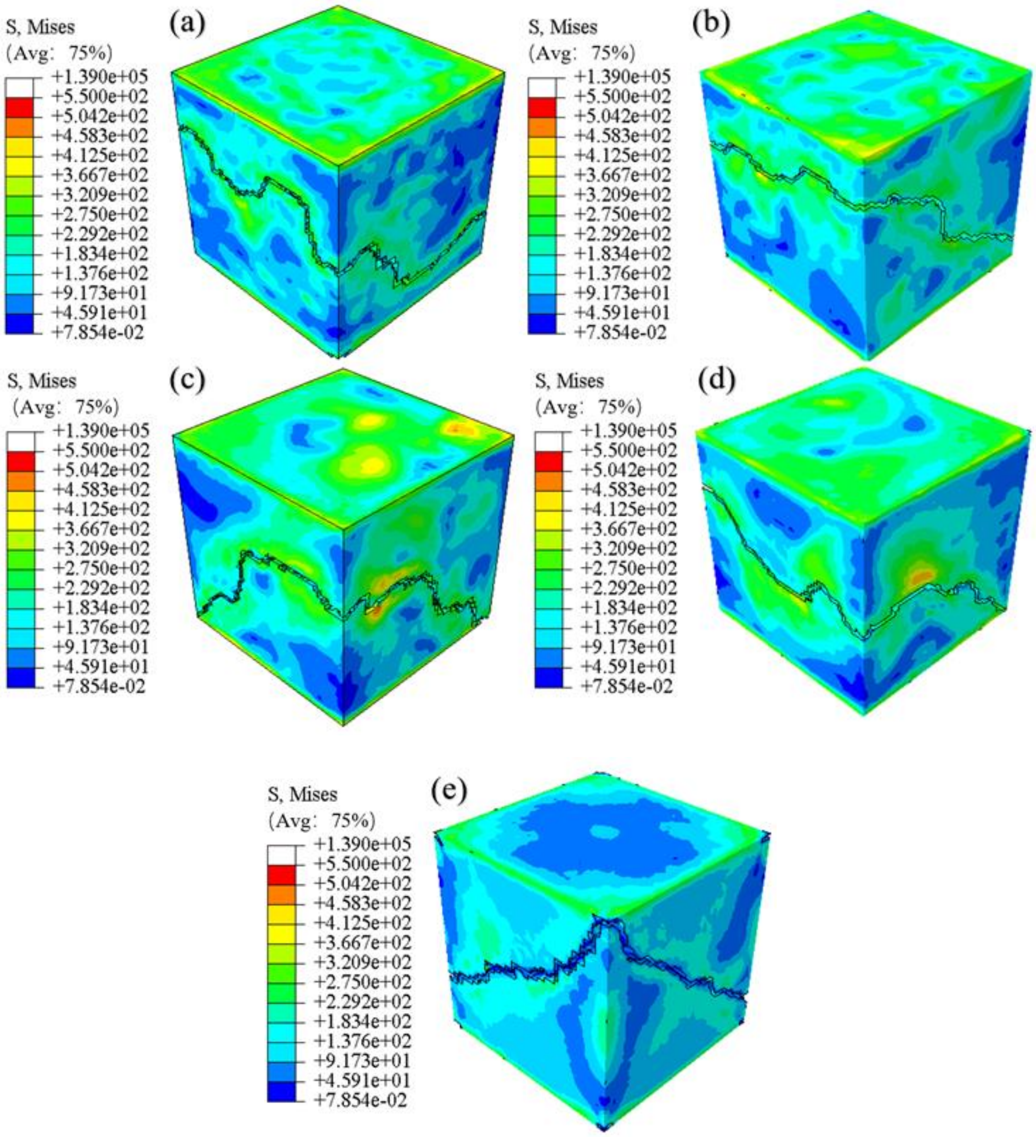

(a) matrix damage diagram with an equivalent particle size of 5μm

(b) matrix damage diagram with an equivalent particle size of 10μm

(c) matrix damage diagram with an equivalent particle size of 15μm

(d) matrix damage diagram with an equivalent particle size of 20μm

(e) damage diagram of the AZ91D matrix

Fig. 3.18. Matrix damage of SiC/AZ91D composites under uniaxial compression with different equivalent particle sizes.

Fig. 3.18 (a), fig. 3.18 (b), fig. 3.18 (c), and fig. 3.18 (d) show the matrix damage under uniaxial compression of composite materials with equivalent particle sizes of 5μm, 10μm, 15μm, and 20μm, respectively. Fig. 3.18 (e) shows the matrix damage under uniaxial compression of pure AZ91D matrix. It can be seen from the figure that the angle between the compression section of the matrix and the loading direction is about 45°. This phenomenon can be explained by the shear stress formula (33) in metal compression deformation[60]:

$$\tau = \frac{\sigma}{2}\sin 2\alpha \tag{33}$$

Where τ is shear stress, σ is allowable stress, and α is the angle between the cross-section's outer normal and the oblique section's outer normal. According to the formula, when α=45°, $\sin 2\alpha$=1, the shear stress τ reaches the maximum value. It can be seen that the sample has the maximum shear stress on the cross-section, which is about 45° with the axis during compression, so the failure section and the axis are about 45° angle.

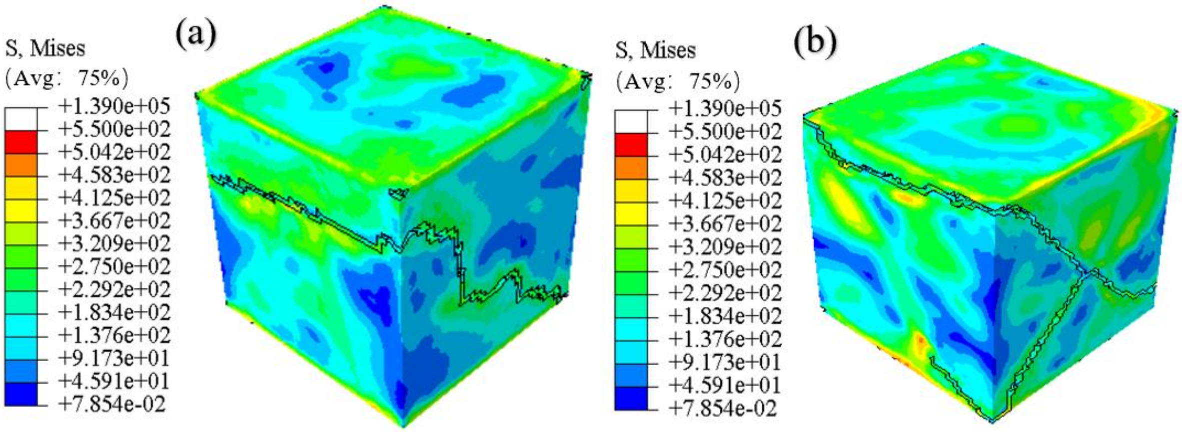

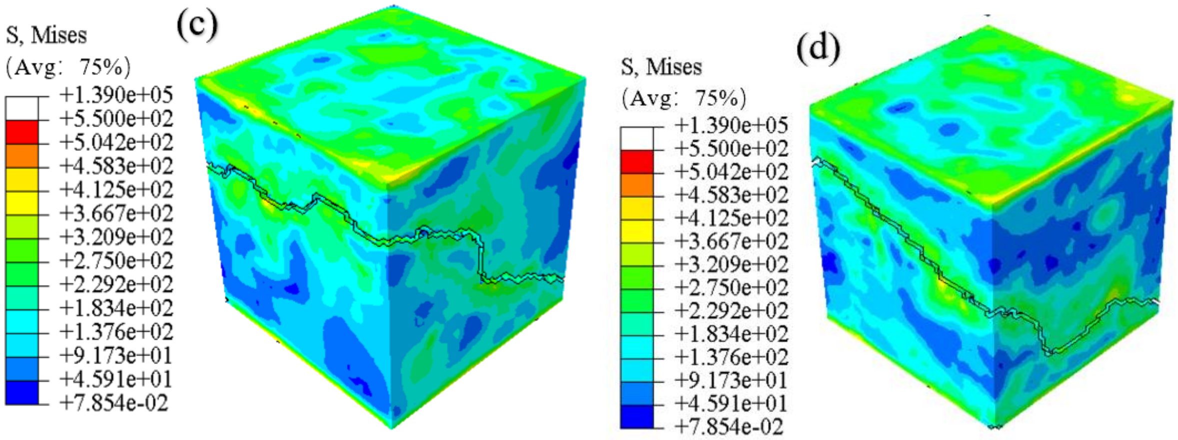

(a) matrix damage diagram with a volume fraction of 5%

(b) matrix damage diagram with a volume fraction of 10%

(c) matrix damage diagram with a volume fraction of 15%

(d) matrix damage diagram with a volume fraction of 20%

Fig. 3.19. Matrix damage of SiC/AZ91D composites under uniaxial compression with different particle volume fractions.

Fig. 3.19 (a), fig. 3.19 (b), fig. 3.19 (c), and fig. 3.19 (d) show the matrix damage under uniaxial compression of composites with particle volume fractions 5%, 10%, 15%, and 20%, respectively. It can be seen from the figure that the angle between the compression section of the matrix and the loading direction is about 45°, which can be explained by the shear stress formula (33) above.

Fig. 3.20 (a), fig. 3.20 (b), fig. 3.20 (c), and fig. 3.20 (d) show the matrix damage under uniaxial compression of composites with circular, primitive, and square particle shapes, respectively. It can be seen from the figure that the angle between the compression section of the matrix and the loading direction is about 45°, which can be explained by the shear stress formula (33) above.

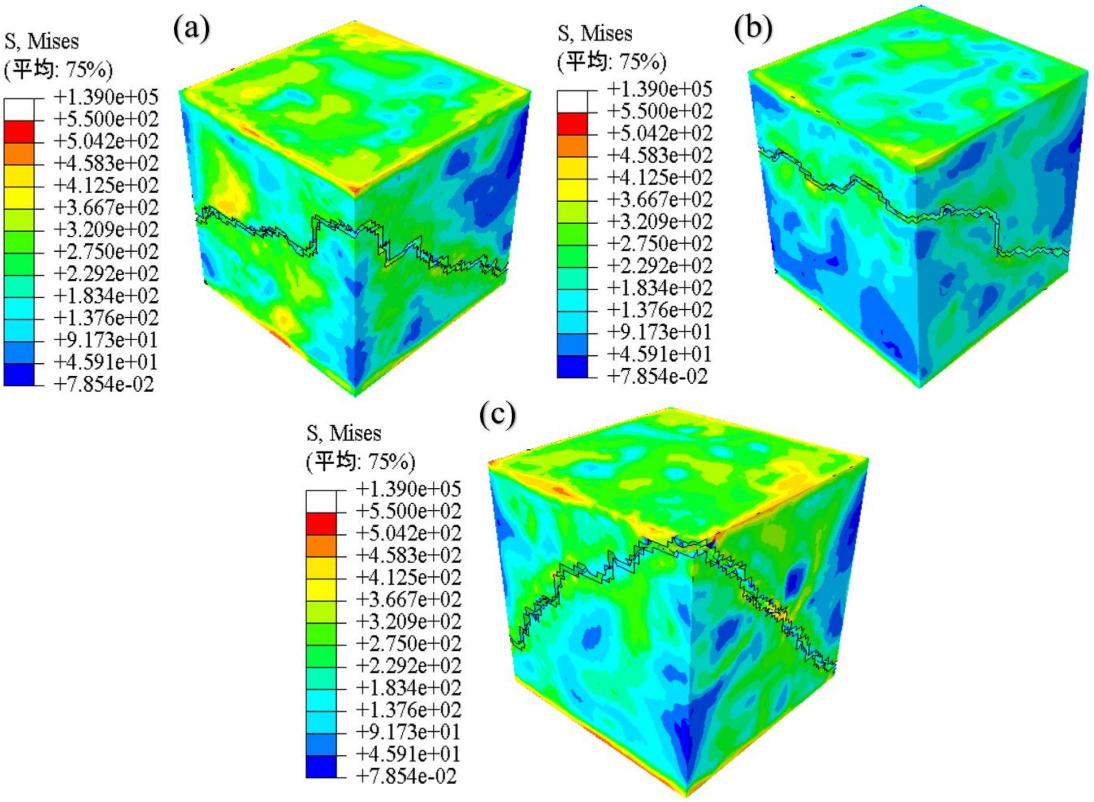

(a) matrix damage diagram with circular particle shape

(b) matrix damage diagram with the original particle shape

(c) matrix damage diagram with the square particle shape

Figure3.20 Matrix damage of SiC$_p$/AZ91D composites under uniaxial compression with different particle shapes

Summary of this chapter

A three-dimensional microstructure-based finite element model was developed to predict the crack sprouting extension mechanism of SiC$_p$/AZ91D composites with different particle equivalent particle sizes, different particle volume fractions, and different particle shapes.

4 . EXPERIMENTAL DEMONSTRATION

4.1 Fracture morphology

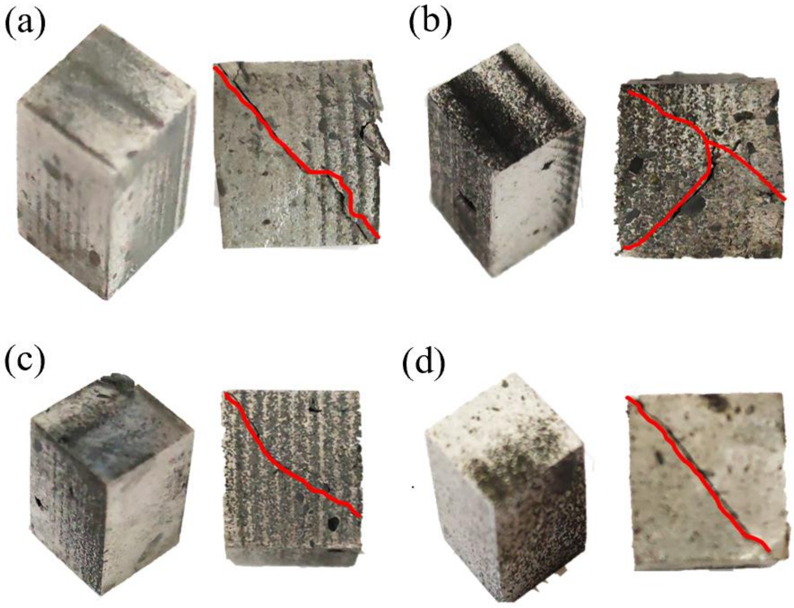

(a) Fracture diagram with a volume fraction of 5%

(b)Fracture diagram with a volume fraction of 10%

(c)Fracture diagram with a volume fraction of 15%

(d)Fracture diagram with a volume fraction of 20%

Fig. 4.1. Fracture diagram of compressed SiC/AZ91D composites with different particle volume fractions.

Fig. 4.1 shows the morphology of a fractured sample of SiC/AZ91D composites with different particle volume fractions after quasi-static compression. As can be seen from the figure, the experimental samples show significant shear failure characteristics. The cube sample breaks into two pieces along the direction of about 45° relative to the loading direction. The experimental results are consistent with the simulation results in fig. 3.19 (a), fig. 3.19 (b), fig. 3.19 (c), and fig. 3.19 (d).

4.2 Crack extension

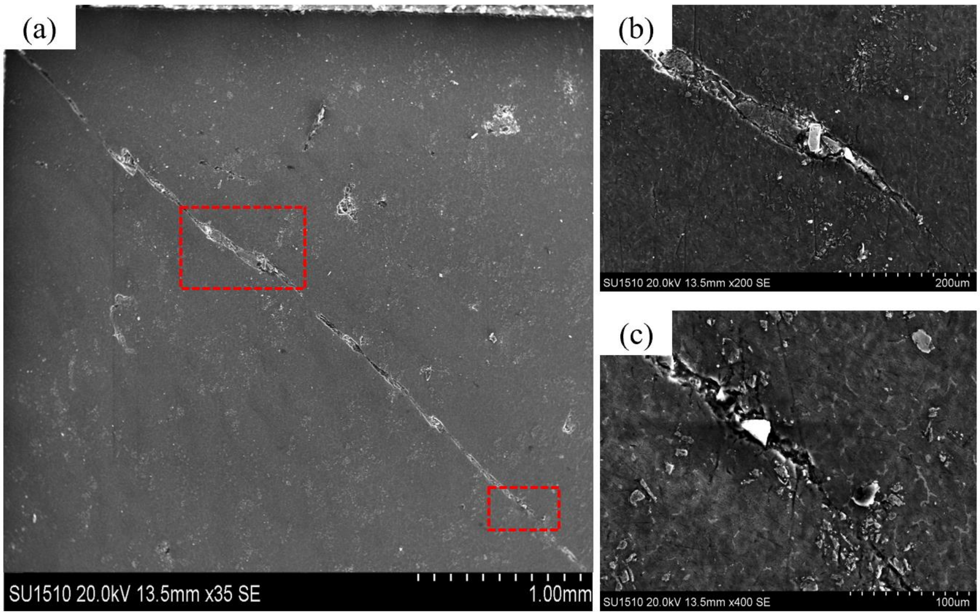

(a) Local full view of crack extension (b) Detailed view of 200μm in the upper left box (c) Detailed view of 100μm in the lower right box

Fig. 4.2. SEM image of the crack in the SiC_p/AZ91D composites.

Fig. 4.2 shows the crack extension under the scanning electron microscope of the tungsten filament of the composite material, fig. 4.2 (a) shows the partial full view of the crack extension, fig.4.2 (b) the 200 μm detailed shape of the upper left box, and fig. 4.2 (c) the 100μm detailed shape of the lower right box. As can be seen from the figure, due to the high breaking strength of the SiC particles, the crack expansion driving force is not sufficient to destroy the SiC particles, and can only expand along the perimeter of the particles, and the presence of the particles plays an obvious role in nailing and hindering the crack expansion. The microcracks are interconnected around the particle periphery expansion and expand along the direction of maximum tangential stress (about 45° relative to the loading), which converge to become the main crack.

4.3 Mechanical properties

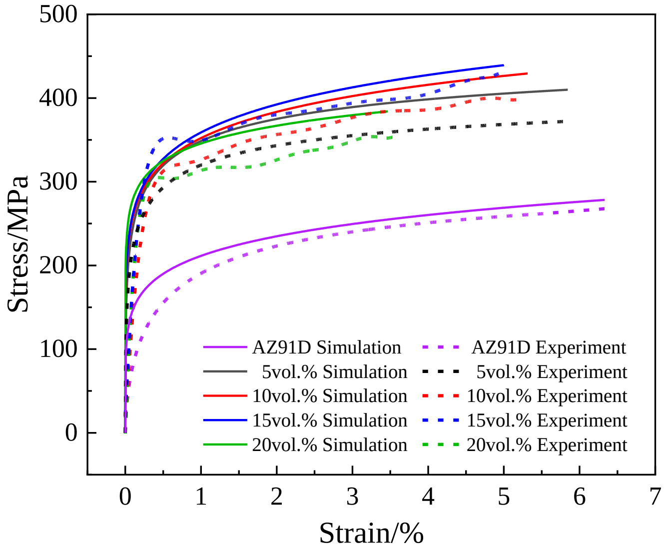

—— Simulated stress-strain curve --- experimental stress-strain curve

Fig. 4.3. Comparison of experimental and simulated stress-strain curves of SiC$_p$/AZ91D composites with different volume fractions.

The standard of whether the obtained simulation curve is good or bad is that, under the condition of the same number of parameters, the closer the simulated curve value $\{\hat{y}\}$ is to the experimental curve value {y}, the better the curve fit is. Therefore, referring to reference [61], a goodness-of-fit index R_{NL} is introduced as:

$$R_{NL} = 1 - \sqrt{\frac{\sum(y_i - \hat{y}_i)^2}{\sum y_i^2}} \tag{34}$$

Among them, $\sum(y_i - \hat{y}_i)^2$ is the residual squared, and $\frac{\sum(y_i - \hat{y}_i)^2}{\sum y_i^2}$ is the relative error. For the data provided by the original data and the fitted curve, it is clear that there is $R_{NL} \leq 1$. R_{NL} organically combines the residual sum of squares and the relative error with clear geometric meaning and simple calculation; the closer R_{NL} is to 1, the better the curve fit.

It can be seen from the data in fig. 4.3 and (34) that in the online elastic stage, the goodness of fit R_{NL} is 0.952, and the simulation results are in good agreement with the experimental results; in the yield stage, the goodness of fit R_{NL} is 0.896, and the simulation and experimental results are slight deviations, which may be caused by defects in the composite microstructure that are not considered in the model.

Summary of this chapter

In summary, the simulation results are in good agreement with the experimental results, and the simulation model and its analysis results in this paper are credible and reliable.

5 . ENVIRONMENTAL PROTECTION

Metal matrix composites have more desirable application advantages than ordinary metal materials, especially particle-reinforced metal matrix composites, which have a level of performance that is difficult to achieve with ordinary composites, such as strong wear resistance and high-temperature resistance, etc. Therefore, they are currently being focused on research and development and are worthy of in-depth investigation and development.

Metal matrix composites are a new type of high-technology engineering material that has been developed rapidly in recent years. It has high specific stiffness and strength, excellent high-temperature performance, low coefficient of thermal expansion, and good wear resistance and friction reduction. Due to its excellent processing and forming properties and obvious performance-to-price advantages, its research and application development is being carried out in many countries around the world, such as the United States, the United Kingdom, Japan, India, and Brazil, on a large scale at many levels. The successful application of metal matrix composites is firstly in the field of aviation and aerospace, for example, NASA uses boron aluminum composites to manufacture the 20 m long cargo hold truss in the middle of the aircraft; Martin uses titanium diboride particle-reinforced aluminum matrix composites to manufacture the wing. In recent years metal matrix composites have been increasingly used for key components requiring greater precision. British Aerospace has been researching the use of particle and whisker-reinforced aluminum alloys for Trident missile guidance components since the 1980s, and DWA and BP have produced composite sheets and profiles for aircraft and missiles, as well as aerospace structural guides. As research into composites progresses, their applications are beginning to expand from the military (aircraft and missile components) to civil (automotive, motorbike, textile, petroleum, chemical, and other industries), and they have very promising applications in manufacturing in particular.

5.1 Application of Metal Matrix Composites

5.1.1 Metal matrix composites for aerospace applications

Fig. 5.1. Metal matrix composite aerospace components.

The main areas of application for metal matrix composites are in the aviation, aerospace, and military sectors, and have been successfully used in artificial satellite mounts, L-band planar antennas, space telescopes, camera waveguides, mirror barrels, infrared mirrors, parabolic antennas for artificial satellites, etc. In the aerospace industry, NASA's LEWIS research center is developing advanced gas turbine engines for aviation using metal matrix composites. The US DWA special composites company uses 25% silicon carbide 6061 aluminum composite material instead of 7075 aluminum to manufacture aviation structure guide channel and angle material. The development goal is to replace aluminum alloys, titanium alloys, steel, etc. for the manufacture of high-performance components, reducing weight and improving performance and instrument accuracy. In the USA, aluminum carbide composite profiles with a mass of 182 kg have been extruded from φ455 mm billets and rolled to a size of 3 050 mm x 1 320 mm x 3 mm for the manufacture of parts for rocket motors, missiles, and satellites. Her cast Canada has piloted particle-reinforced aluminum (PRA) composite materials for precision castings such as optical bases and universal brackets, as well as hydraulic tubes, pressurized volutes, and satellite reaction wheels, replacing aluminum alloys, reducing weight and improving performance. DWA replaced aluminum alloy with silicon carbide particle-reinforced 6092 aluminum matrix composites on a large scale for the vertical tail fin of the F16 fighter jet, increasing service life by 17 times; and replaced resin matrix composites for the P&W4000 engine fan exit guide vanes of the Boeing 777, significantly increasing service life and reducing costs by 33%. DWA (USA) and AMC (UK) have used aluminum carbide composites in bulk for the EC-120 and EC-135 helicopter rotor systems, significantly increasing component stiffness and service life. The successful application of these key structural components demonstrates the maturity of research into the application of this material in the US and UK[62].

5.1.2 Metal matrix composites for automotive

The main metal matrix composites used in the automotive industry are particle-reinforced and short fiber-reinforced aluminum and magnesium composites. Currently, aluminum matrix composites are usually made of aluminum-silicon alloys. Commonly used filler reinforcements include ceramic fibers, whiskers, and particulates. Compared with aluminum alloys, aluminum matrix composites have the advantages of being lightweight, having high specific strength and modulus of elasticity, and good heat resistance, and wear resistance, making them ideal for lightweight automotive applications. High-performance aluminum pistons made of low-density metal and reinforced ceramic fibers are currently being used. Aluminum pistons with aluminum oxide fiber reinforced piston tops, pistons made of aluminum oxide reinforced magnesium alloys, aluminum oxide fiber, and stainless steel fiber-reinforced aluminum matrix composite rods have been introduced abroad, further expanding the application of composite materials in pistons. Aluminum matrix composites are also used in brake wheels, which are characterized by a mass reduction of 30% to 60% and good thermal conductivity. An American automobile company has developed a brake wheel made of aluminium-10% silicon-magnesium matrix composite reinforced with silicon carbide particles. At present, China's SAIC Group has cooperated with relevant universities to research and develop aluminum-based composite car brake discs, which will be used in SAIC's independently developed car brake system with independent intellectual property rights [63].

5.1.3 Industrial, recreational, and infrastructure industry sectors

Other applications for metal matrix composites cover the manufacturing, optical instrumentation, electronics, sports and leisure, and infrastructure sectors, and include established markets such as hard alloys, electroplated and sintered diamond tools, copper and silver-based electrical contacts, as well as emerging areas such as titanium carbide-reinforced iron-based wear-resistant materials, aluminum trioxide fibre-reinforced aluminum-based power transmission cables, and aluminum tetraboron carbide-reinforced neutron absorbers. The performance of these emerging areas will largely determine the future growth of metal matrix composites. The preparation and application of iron matrix composites is an important research direction for improving the performance of steel materials. The addition of low-density, high-stiffness, and high-strength reinforcement particles to the steel matrix reduces the density of the material while increasing its modulus of elasticity, hardness, wear resistance, and high-temperature properties, which can be used in cutting, rolling, shot peening, stamping, piercing, drawing and molding. The most current applications are titanium carbide particle-reinforced iron-based composites such as Ferro-TiC, Alloy-TiC, and Ferro-Titanic steel-based carbides, which are used in anti-wear materials and high-temperature structural materials and offer significantly better performance than existing tool steels. Industrial applications include carbide, cermets, electroplated and impregnated diamond tools, copper and silver metal matrix composite electrical contacts, and corrosion-resistant coatings for the petrochemical industry. Titanium carbide reinforced iron and nickel alloys have excellent hardness and good wear resistance and are used in a wide range of industrial applications: cutting, rolling, pelletizing, stamping, punching, hot metal working, drawing, die forging, drilling, etc.; for parts such as forging hammers, stamping dies, canning tools, embossing rolls, check valves, extruder nozzles, bending dies, extrusion dies, hot forging die liners, etc. Applications for metal matrix composites in the recreational market include competition bicycle tubes, line spikes, and lacrosse sticks. The braking surfaces of bicycle wheel rims are coated with metal matrix composites to improve wear resistance and reduce braking distances. Infrastructure applications include aluminum-tetraboron carbide for nuclear waste and aluminum-aluminum trioxide for overhead cables. Metal matrix composite products can increase power delivery by 200 to 300% and can have significant economic benefits if they are widely used in infrastructure grids [64].

5.2 Metal matrix composites waste recovery method

When metal matrix composite scrap cannot be recycled, or cannot be made into commercially viable composites due to the presence of high levels of oxidation inclusions, separation methods can be used to remove the reinforcement from the composite and turn it back into valuable metal. There is currently limited literature on the remelting and recycling of particle-reinforced metal matrix composites. Only Canadian companies and researchers in the USA have conducted international research on remelting and recycling of composites, but the results have not been satisfactory. There are several methods for recycling metal matrix composites:

5.2.1 Molten salt treatment

During remelting of composites, to avoid absorption and dissolution of hydrogen by the melt and to prevent the involvement of oxidation inclusions. The American company uses Ar gas protection[65]. A graphite stirrer driven by a pneumatic motor was used for slow stirring to prevent sinker segregation. The study[66] pointed out that granular reinforced metal matrix composites cannot be refined with the refining de-gasifiers of common alloys and that to reduce gas inclusions in the granular metal matrix composites, the company designed an extensive pouring system and filtering and dross removal system, which resulted in dense castings but too low casting yields and material utilization. The researchers studied the remelting recovery of composites showing that salt refining agents and other refining degasifiers common to alloys were used for interfacial de-wetting of composites and that the remelted melt of composites was treated with a second refining agent for refining. The results[67] showed a greater loss of densification dose, reduced densification effect, introduction of elements into the melt, interfacial de-wetting, and reduced volume fraction. The effect of grain refiners on the densification and refining of the composite was found to be significant, except for the densifier, which was found to be suitable for the composite, and the densifier and grain refiners were found to cause deliquescence and sinking when used on the composite.

5.2.2 Rotary oven method

The conventional rotary furnace method[68,69] is used for the recovery of composite materials. For the same amount of molten salt addition, the rotary furnace method is significantly more efficient than the single molten salt method, with recoveries of up to 80%.

5.2.3 Gas injection and plasma furnace method

The advantages of this method are the smaller amount of molten salt required and the higher efficiency of recovery, thus avoiding the problem of insoluble molten salt, in addition to the fact that this method allows the recovery of reinforcing particles [69].

Summary of this chapter

So far, although some composite products have been produced, the problem of recycling and recovery of metal-based composites has not been solved, and this may be one of the reasons why the material has not entered into the application so far. Therefore, it is important to strengthen the basic and applied research on remelting, recycling, and recovery of composite materials.

The sustainable development of composite materials and the need for their practicality and cost reduction make the issue of metal-based composite material recycling particularly important.

1. more effective measures to control the interfacial behavior of the reinforcement and the matrix during the remelting process
2. to explore in depth the regimes and regeneration mechanisms for the remelting of metal-based composite materials.

6 . LABOR PRECAUTION

The processes of human activity take place in close interaction and are shaped by the productive environment that shapes the productive environment. In other words, the working environment affects a person's working processes and thus a person. The working processes of a person, and thus his health and ability to work, are the working conditions. This section discusses workplace manufacturing safety and health-related issues for alloy production workers in all phases of designing, casting, and melting magnesium matrix composites [70].

The main task of occupational safety is to create safe and healthy working conditions for employees and to improve the creation of a safe working environment. The organization of labor protection measures in metal smelting enterprises can only be carried out safely at a high level if an occupational safety approach is used. Strict compliance with labor laws, guidelines, industry standards, rules, and regulations aimed at protecting the health of workers is necessary, the most important of which is the corresponding action by the administration to organize the implementation of labor protection requirements, the enforcement of labor protection requirements and the labor and production discipline of the employees themselves[71]. The production processes of metal smelting, casting, forging, and heat treatment are accompanied by high temperatures and emit various harmful gases, dust, and fumes, as well as generating noise, thus seriously deteriorating the working environment and working conditions. These operations are characterized by many work processes, heavy physical labor, and a large lifting and transport workload, which makes them prone to various types of injuries and requires the adoption of targeted safety technical measures.

6.1 Analysis of working conditions in the workplace

6.1.2. The microclimate and ventilation

72

Fig. 6.1. Magnesium metal workshop workers feeding material.

Metal smelting operations, such as steel and iron making, are carried out at temperatures of over a thousand degrees. When working at high temperatures, the human body is affected by high temperatures and a series of physiological function changes occur, such as a decrease in body temperature regulation. When the production environment temperature exceeds 34°C, heat stroke can easily occur. If the work is too intense and the duration of work is too long, heat stroke is more likely to occur. In severe cases, it can lead to shock [73].

The measures to prevent heat stroke are to design the process rationally, improve production equipment and operating methods, and eliminate or reduce the impact of high temperature and heat radiation on the human body. This is a fundamental measure to improve working conditions at high temperatures. Insulation with water or materials with low thermal conductivity is also an important measure to prevent heat stroke. The use of mechanical ventilation and natural ventilation is an economical and effective way to dissipate heat. At the same time, it is required that employers around the world should, according to the production characteristics and specific conditions during hot weather, appropriately adjust the labor and rest system of summer high-temperature work while ensuring the quality of work, increasing rest and reducing labor intensity, reduce work during high-temperature periods, ensure safe production, and ensure the health and life safety of workers [74].

6.1.2 Explosion and scalding

Fig. 6.2. Liquid metal splash.

Foundry to improve efficiency, and reduce consumption, often using measures to strengthen smelting, such as coal dust and blowing oxygen, which makes the casting production prone to metal spatter and explosion accidents[75].

The causes of metal spatter, and the explosion for many reasons, from raw materials to the production of steel, iron, and the entire production process, are hidden unsafe factors. Preventive measures must be strengthened in each process.

- The personnel in each production position must master the laws of production, be familiar with the operating procedures, carefully observe the precursors of accidents and know how to deal with them.
- Strengthen the management and selection of raw materials to prevent explosives and sealed containers from entering the furnace.
- Check the cooling system frequently to protect the system from flowing smoothly. Control the cooling water pressure and water volume to prevent insufficient strength of the water cooling system from causing the furnace to burn through, resulting in an explosion of the molten metal liquid in contact with water.
- The production workshop should strictly implement the hot air furnace working system to prevent the hot air furnace from exploding due to the furnace change accident; the refining workshop should strictly implement the operating procedures of the whole production process from furnace replenishment, furnace loading, melting to steel discharge to avoid spattering and explosion accidents in the melting process due to improper operation.
- When casting and forming, heat and dry the iron ditch, iron tank, ladle, pit, and ingot mold beforehand. Prevent explosions caused by humidity.

6.1.3 Gas poisoning

Fig. 6.3. Exhaust emissions.

The main harmful component of gas is carbon monoxide. The waste gas produced in metal smelting production, especially in iron production, i.e. blast furnace gas, contains high levels of carbon monoxide and is therefore prone to gas poisoning accidents if not handled properly in steel and iron production. An effective way to prevent this is to pay attention to strengthening ventilation, monitoring, maintenance, and personal protection at the production site.

Statistics from countries around the world have shown for many years that carbon monoxide (CO) has become the most common toxic and hazardous gas, with a large number of CO poisonings occurring each year and a high mortality rate. Carbon monoxide poisoning occurs in a wide range of environments. In industrial production dozens of different production industries or environments have operations that can come into contact with carbon monoxide (CO), such as incomplete combustion of carbonaceous substances in ironmaking, coking, casting, and heat treatment in the metallurgical industry; the production of synthetic ammonia, phosgene, methanol, acetone and other gases in the chemical industry can also produce carbon monoxide; carbon graphite electrode manufacturing; mine shelling, gas explosion accidents; commissioning of internal combustion engines; processes for the production of metal carbonyls [76].

In addition to industrial production, the use of combustible gases containing CO can also be exposed to carbon monoxide, such as water gas containing CO up to 40% or more, blast furnace and furnace gas containing 30%, a gas containing 5% to 15%; internal combustion engine using diesel or gasoline exhaust gas also contains carbon monoxide about 1% to 8%, and explosives or gunpowder after the explosion of the gas also contains carbon monoxide 30% to 60%.

According to statistics, acute occupational poisoning is the most common cause of morbidity and mortality in our country, and not only that, but it is also the most common cause of accidental poisoning deaths in many countries around the world. Studies have shown that the cause of carbon monoxide poisoning is related to the concentration of carbon monoxide to which the patient is exposed and the duration of exposure. In China, the maximum concentration of carbon monoxide in workshop air must not exceed 25ppm, while data shows that when in the air with a carbon monoxide concentration of 200ppm for 3 hours, the carboxyhemoglobin in human blood will exceed 10%; when the concentration of carbon monoxide reaches 250ppm, the carboxyhemoglobin content will reach 25%, which will cause severe headache and dizziness; when in When breathing in air with a carbon monoxide concentration of 800 ppm for 60 minutes, the carboxyhemoglobin level in the blood can reach 60%, causing a coma; and once the carbon monoxide concentration reaches 10,000 ppm, the carboxyhemoglobin level in such an environment can reach 90%, which can cause death in a few minutes [77].

No matter what kind of air contains carbon monoxide occasions, generally have to install a carbon monoxide detector, when people go in and out of the low concentration of carbon monoxide site, if the site is not installed carbon monoxide detector, you can take a portable carbon monoxide detector into, with the monitoring site carbon monoxide concentration, and in some high concentration of carbon monoxide site, the installation of a carbon monoxide alarm is very necessary, real-time remote monitoring of the site carbon monoxide concentration, so that the concentration exceeds the standard can be made promptly corresponding measures to deal with, to avoid the site personnel poisoning events.

6.2 Fire safety

6.2.1 Fire protection measures

The fire protec

- Plants and buildings must be equipped with fire-fighting facilities.
- The production site should be equipped with suitable fire extinguishing agents such as powdered No. 2 melt and covering agents for production, dry magnesium sand or dry sand, asbestos sheets or asbestos cloth, etc. The refinery should also be equipped with a special Class D fire extinguisher.
- The use of water, foam, carbon tetrachloride, and carbon dioxide extinguishing agents is prohibited for burning magnesium and magnesium alloys.

6.2.2 Fire design objectives

For critical fire protection areas in steel and metallurgical enterprises, the design objectives should be formulated in terms of "preventing fires from occurring; quickly detecting and extinguishing fires that have already occurred, and mitigating fires by preventing the spread of fires that have not yet been extinguished". "Fire prevention" is the requirement to minimize the probability of fires in the operation of steel and metallurgical enterprises and requires fire protection design to be considered in conjunction with process and production management. "Rapid detection and extinguishing of fires that have already occurred" is a requirement to reduce fire damage by using active firefighting techniques such as automatic and semi-automatic fire protection to achieve early detection and early extinguishing of fires. "Mitigation of fires by preventing the spread of fires that have not yet been extinguished" is a requirement to use passive fire separation to delay or stop the development of fires and gain time for rescue.

6.2.3 Fire protection design elements

First, the fire prevention part of the building. It should be closely integrated with the actual situation of iron and steel metallurgical enterprises, and the fire hazards of each building (structure) and process facilities should be comprehensively, exhaustively, and scientifically classified, and considered from the aspects of safe evacuation and building construction. Secondly, the fire protection design of the processing system is a key concern in industrial fire protection. First, determine the key fire protection areas in the processing system and the main buildings (structures) and facilities in the area, and according to the classification of fire hazards, take corresponding fire protection measures to avoid starting fires, reduce the chance of burning and control the spread of fire burning. Secondly, to determine the measures and facilities necessary for the rescue of personnel in the event of a fire and to ensure that firefighters can enter the premises to fight the fire. Finally, the process requirements are to determine whether to activate the automatic fire extinguishing system in the event of a fire. Automatic fire extinguishing systems should be combined with process safety factors to determine the appropriate start-up and exit times. Thirdly, the fire alarm, smoke control, and fire protection electrical systems are part of the system. Consideration is given to active fire protection and fire protection system work security [79].

6.2.3 Unified Planning

Due to the internal development needs of steel and metallurgical enterprises, there are a large number of new construction, alteration, and expansion projects every year. These projects are built at different times and according to different construction standards, resulting in inconsistent fire safety assurance capabilities for each process system. Due to the nature of process production in iron and steel metallurgical enterprises, any unsafe part of the production process may lead to the failure of other systems.

6.2.4 Fire safety assessment

Fire safety in steel and metallurgical enterprises is a broad concept that involves many aspects, the most important being that the production process is closely linked to the occurrence of fire. On the one hand, fires can cause damage and direct and indirect losses to important items or processes in industrial enterprises; on the other hand, factors of process safety can cause fires and further damage. Fire safety and production safety are therefore inseparable and require a comprehensive fire safety assessment in conjunction with process safety factors.

Summary of this chapter

- It should implement and enforce the relevant laws and regulations, strengthen the management of production safety, establish and improve the system of responsibility for production safety, improve the conditions of production safety and ensure safe production. The legal person of the enterprise should identify and review the major sources of danger and occupational hazards such as explosions, fires, and toxic factors in the enterprise by the relevant regulations, determine the types of hazardous factors, and the degree of hazard, and formulate effective management and control measures. Managers should conduct safety inspections with members of the safety organization to correct unsafe operations and environments to bring them into compliance with the relevant regulations. Smoking and frolicking should not be allowed on the production site, and no alcohol or sickness should be allowed in the workplace. Specialized equipment should be operated by dedicated personnel.
- The enterprise should formulate rules for the implementation of safety measures and safety checklists for the enterprise, taking into account the characteristics of production, and carry out inspections carefully according to the safety checklists. The enterprise should be inspected at least once a month and the workshop at least

once a week. Enterprises should seriously educate themselves on production safety, popularise safety knowledge and safety regulations, and enable employees to understand the safety production characteristics of their enterprises. Employees should be trained in their professional skills and knowledge of safety products and be qualified to work after the examination.

GENERAL CONCLUSIONS

The agreement of the experimental stress-strain curves and fracture morphology with the simulation predictions proved the validity of the modeling results. Some of the important conclusions drawn from our work are summarized as follows:

(1) Crack germination of SiC_p/AZ91D composites with different equivalent particle sizes mainly appeared at the sharp corners of particle edges and in the matrix between particles. The larger the equivalent particle size is, the more serious the crack propagation degree is. The microcrack first initiates at the junction of the particle and matrix. It then expands around the boundary or sharp corner of the SiC particle along the direction of maximum shear stress, forming the main crack. The increase in equivalent particle size will

accelerate the composites' crack germination and propagation fracture process.

(2) The sharper the particle shape, the lower the compressive strength of the composite. Round particle composites fracture the slowest, primitive shape particle composites fracture the second, and square particle composites fracture the fastest.

(3) The existence of SiC particles has a pronounced blocking effect on crack growth. The crack expands along the path with the maximum shear stress, and increasing particle volume fraction will accelerate the crack germination and fracture process of composite materials.

(4) Compared with the matrix alloy, the yield strength and compressive strength of SiC_p/AZ91D composites with different equivalent particle sizes and different volume fractions are significantly increased, while the plasticity is decreased. The smaller the equivalent particle size is, the higher the compressive strength is and the better the plasticity is. With the increase of particle volume fraction, the compressive strength of the composites increases first and then decreases, and the plasticity decreases continuously.

(5) The angle between the standard line of the AZ91D matrix compression section and the loading direction of the AZ91D matrix with different equivalent particle sizes and volume fractions is about 45°, which is because the sample has the maximum shear stress on the cross-section with approximately 45° of the axis during compression.

REFERENCES

[1] Zhang Jiangtao. Experimental Study and Numerical Simulation of Dynamic Mechanical Properties of Particle Reinforced Metal Matrix Composites. PhD Thesis. Wuhan:Wuhan University of Technology, 2007.

[2] Gui Manchang. Research, development and application of particle-reinforced aluminum matrix composites. Jiangsu Science and Technology Information. 2002, 3:22-24.

[3] Tengke Ye, et al."Effects of SiC particle size on mechanical properties of SiC particle reinforced aluminum metal matrix composite." Materials Science & Engineering A 753.(2019). https://doi.org/10.1016/j.msea.2019.03.037.

[4] Yi Wang, Yushi Meng, Punyawut Jiradilok, Koji Matsumoto, Kohei Nagai, Shingo Asamoto,Expansive cracking and compressive failure simulations of ASR and DEF damaged concrete using a mesoscale discrete model,Cement and Concrete Composites,Volume 104,2019, 103404,ISSN 0958-9465,https://doi.org/10.1016/j.cemconcomp.2019.103404.

[5] Ronghua Chen, Bochuan Li, Kang Xu, Effect of particle morphology on fatigue crackpropagation mechanism of TiB2-reinforced steel matrix composites,Engineering FractureMechanics,Volume 274,2022,108752,ISSN 0013-7944,https://doi.org/10.1016/j.engfracmech.2022.108752.

[6] Editorial Committee of "New Materials for High Technology", New Materials for High Technology [M]. Beijing: China Science and Technology Press 1993, 4~99.

[7] The Executive Committee of the Second Annual Youth Academic Conference of the Chinese Association for Science and Technology, ed. Progress and Prospects in Materials Science and Technology [C] Beijing: China Science and China Science and Technology Press, 1995, 6: 41~46.

[8] Akeem Damilola Akinwekomi, Wing-Cheung Law, Chak-Yin Tang, Ling Chen, Chi-Po-ng Tsui,Rapid microwave sintering of carbon nanotube-filled AZ61 magnesium alloy composites,Composites Part B: Engineering,Volume 93,2016,Pages 302-309,ISSN 1359-8368,https://doi.org/10.1016/j.compositesb.2016.03.041.

[9] Mingjie Shen, Baojian Han, Tao Ying,Micromechanical simulations and experimental c-haracteristics of randomly distributed carbon nanotubes reinforced Mg matrix composites,Journal of Alloys and Compounds,Volume 924,2022,166589,ISSN 0925-8388,https://doi.org/10.1016/j.jallcom.2022.166589.

[10] Tengke Ye, et al."Effects of SiC particle size on mechanical properties of SiC particle reinforced aluminum metal matrix composite." Materials Science & Engineering A 753.(2019). https://doi.org/10.1016/j.msea.2019.03.037.

[11] Yi Wang, Yushi Meng, Punyawut Jiradilok, Koji Matsumoto, Kohei Nagai, Shingo Asamoto,Expansive cracking and compressive failure simulations of ASR and DEF damaged concrete using a mesoscale discrete model,Cement and Concrete Composites,Volume 104,2019, 103404,ISSN 0958-9465,https://doi.org/10.1016/j.cemconcomp.2019.103404.

[12] Ronghua Chen, Bochuan Li, Kang Xu, Effect of particle morphology on fatigue crackpropagation mechanism of TiB2-reinforced steel matrix composites,Engineering FractureMechanics,Volume 274,2022,108752,ISSN 0013-7944,https://doi.org/10.1016/j.engfracmech.2022.108752.

[13] Liu W. Numerical simulation of two-dimensional crack expansion and fatigue life prediction [D]. Shandong University,2014.

[14] Cheng Jin, Zhao Shushan. Fracture mechanics [M]. Beijing:Science Press, 2006.

[15] ARSENAULT R.J., FISHMAN S., TAYA M. Deformation and fracture behavior of metal-ceramic matrix composite materials J. Progress in Materials Science, 1994,38:1-157.

[16] PENG Peng. Mechanical properties and 3D fi-nite element mechanical simulation of B4Cp/6061Al composites [D]. Dalian Universi-ty of Technology, 2021.

[17] RAHIMIAN M.,EHSANI N.,PARVIN N.,et al. The effect of particle size,sinteringtemperature and sintering time on the properties of Al-A12O3 composites,made by powder metallurgy I. Jour-nal of Materials Processing Technology，2009, 209:5387-5393.

[18] CUI Yan, NI Haochen, CAO Leigang, YANG Yue, WANG Yiming. Effect of SiC particle shaping on mechanical properties of high-volume aluminum matrix composites and finite element simulation[J]. Materials Review, 2019,33(24):4126- 4130.

[19] LI Kun, JIN Xiaodong, YAN Benda, LI Pengxing. Effect of SiC particle volume fraction on fatigue crack growth of SiCp/Al composites [J]. Journal of Composite Materials, 1992(02):83-88.

[20] Azra Rasool, Helmut J. Böhm,Effects of particle shape on the macroscopic and microscopic linear behaviors of particle reinforced composites,International Journal of Engineering Science, Volume 58,2012,Pages 21-34,ISSN 0020-7225,https://doi.org/10.1016/j.ijengsci.2012.03.022.

[21] Liu Peng.Effects of particle size,particle distribution and mixture of TiN and TiC reinf-orcement on the mechanical property of iron matrix composites[D].Shenyang:Northeastern University, 2015.

[22] Yishi Su, Qiubao Ouyang, Wenlong Zhang, Zhiqiang Li, Qiang Guo, Genlian Fan, Di Zhang, Composite structure modeling and mechanical behavior of particle reinforced metal matrix composites,Materials Science and Engineering: A,Volume 597,2014,Pages 359-369,ISSN 0921-5093,https://doi.org/10.1016/j.msea.2014.01.024.

[23] Jie Zhang, Qiubao Ouyang, Qiang Guo, Zhiqiang Li, Genlian Fan, Yishi Su, Lin Jiang, Enriq

ue J. Lavernia, Julie M. Schoenung, Di Zhang,3D Microstructure-based finite element modeling of deformation and fracture of SiCp/Al composites,Composites Science and Technology,Volume 123,2016,Pages 1-9,ISSN 0266-3538,https://doi.org/10.1016/j.compscitech.2015.11.014

[24]BELYTSCHKO T, BLACK T. Elastic crack growth in finite elements with minimal remeshing[J]. International Journal for Numerical Method in Engineering, 1999, 45(5): 601－620.

[25]MOSE N, BELYTSCHKO T. Extended finite element method for cohesive crack growth[J]. Engineering Fracture Mechanics, 2002, 69(7): 813－833.

[26]BELYTSCHKO T, GRACIE ROBERT. On XFEM applications to dislocations and interfaces [J]. International Journal of Plasticity, 2007, 23(10－11): 1721－1738

[27]MOES N, DOLBOW J, BELYTSCHKO T. A finite element method for crack growth without remeshing [J]. International Journal for Numerical Method in Engineering, 1999, 46(1): 131－150.

[28]Dugdale DS. Yielding of steel sheets containing slits. Journal of the Mechanics and Physics of Solids, 1960, 8: 100-104

[29]Needleman A. A continuum model for void nucleation by inclusion debonding. Journal of Applied Mechanics, 1987, 54: 525-531

[30]Tvergaard V, Hutchinson JW. The relation between crack growth resistance and fracture process parameters in elastic-plastic solids.Journal of Mechanics and Physics of Solids, 1992, 40: 1377-1397

[31]Camacho GT, Ortiz M. Computational modeling of impact damage in brittle materials. International Journal of Solids and Structures,1996, 33: 2899-2938

[32]Geubelle PH, Baylor J. Impact-induced delamination of laminated composites: a 2D simulation. Composites Part B: Engineering,1998, 29: 589-602

[33]Alfano M, Furgiuele F, Leonardi A, et al. Mode I fracture of adhesive joints using tailored cohesive zone models. International Journal of Fracture, 2009, 157: 193-204 16

[34]Martiny PH, Lani F, Kinloch AJ, et al. A maximum stress at a distance criterion for the prediction of crack propagation in adhesivelybonded joints. Engineering Fracture Mechanics, 2013, 97: 105-135 17

[35]Jhin G, Azari S, Ameli A, et al. Crack growth rate and crack path in adhesively bonded joints: Comparison of creep fatigue and fracture. International Journal of Adhesion and Adhesives , 2013, 46: 74-84

[36]Zhang Jun. Application of Interface Stress and Cohesive Zone Model in Interface Mechanics. Zhengzhou: ZhengzhouUniversity Press, 2011

[37] Liljedhal CDM, Crocombe AD, Wahab MA. Damage modeling of adhesively bonded joints. International Journal of Fracture, 2006,141: 147-161

[38] Chen CC, Linzell DG. Modeling end notched flexure tests to establish cohesive element mode II fracture parameters. Engineering Fracture Mechanics, 2010, 77: 1338-1347

[39] Li Weidong, Wu Kunyue,Hu Ping. Study on strength and fatigue behavior of single lap joint under periodic excitation. Chinese Journal of Computational Mechanics, 2014, 31(4): 446-452

[40] Zhang Pan,Xu Yingjie, Wang Haibin, et al. Stress analyses of double lap bonding joint using viscoelastic constitutive model. Applied Mathematics and Mechanics, 2015, 36(2): 160-166

[41] Xu W, Wei Y. Strength analysis of metallic bonded joints containing Defects. Computational Materials Science , 2012, 53: 444-450

[42] Blackman BRK, Hadavinia H, Kinloch AJ, et al. The use of a cohesive zone model to study the fracture of fibre composites and adhesively-bonded joints. International Journal of Fracture, 2003,119: 25-46

[43] Yan Y, Shang F. Cohesive zone modeling of interfacial delamination in PZT thin films. International Journal of Solids and Structures,2009, 46: 2739-2749

[44] Lorena M, Fern C, Sonia S. Influence of the cohesive law shape on the composite adhesively-bonded patch repair behavior. Composites Part B, 2016, 91: 414-421

[45] Cui H. Simulation of ductile adhesive failure with experimentally determined cohesive law. Composites Part B, 2016, Accepted Manuscript.

[46] Jousset P, Rachik M. Comparison and evaluation of two types of cohesive zone models for the finite element analysis of fracture propagation in industrial bonded structures. Engineering Fracture Mechanics,2014, 132: 48-69

[47] Campilho RDSG, Banea MD, Neto JABP, et al. Modelling adhesive joints with cohesive zone models: effect of the cohesive law shape of the adhesive layer. International Journal of Adhesion & Adhesives , 2013, 44: 48-56

[48] Campilho RDSG, Fernandes TAB. Comparative evaluation of single-lap joints bonded with different adhesives by cohesive zone modellin. Procedia Engineering, 2015, 114: 102-109

[49] Sugimura, Y. and Suresh, S. Metall. Trans.Effects of SiC content on fatigue crack growth in aluminum alloys reinforced with SiC particles.A Aug. 1992 23A, (8), 2231–2242,International Journal of Fatigue,Volume 15, Issue 4,1993,Page 342,ISSN 0142-1123,https://doi.org/10.1016/0142-1123(93)90386-5.

[50] Yishi Su,Zan Li,Yang Yu,Lei Zhao,Zhiqiang Li,Qiang Guo,Dingbang Xiong,Di Zhang. Structural modeling and tensile simulation of graphene-reinforced metal matrix composites (in English)[J].Science China Materials,2018,61(01):112-124.

[51] Qiong Xu, Yuhua Li, Hongyan Ding, Aibin Ma, Jinghua Jiang, Guobin Chen, Yegao Chen,Microstructure and mechanical properties of SiCp/AZ91 composites processed by a combined processing method of equal channel angular pressing and rolling,Journal o-f Materials Research and Technology,Volume 15,2021,Pages 5244-5251,ISSN 2238-7854,https://doi.org/10.1016/j.jmrt.2021.11.005.

[52] Abdallah Shokry, Samer Gowid, Ghais Kharmanda,An improved generic Johnson-Cook model for the flow prediction of different categories of alloys at elevated temperaturesand dynamic loading conditions,Materials Today Communications,Volume 27,2021,102296,ISSN 2352-4928,https://doi.org/10.1016/j.mtcomm.2021.102296.

[53] Gordon R. Johnson, William H. Cook,Fracture characteristics of three metals subjectedto various strains, strain rates, temperatures and pressures,Engineering Fracture Mechanics,Volume 21, Issue 1,1985,Pages 31-48,ISSN 0013-7944,https://doi.org/10.1016/0013-7944(85)90052-9.

[54] Zhou Xia, et al. "Numerical simulation of dynamic mechanical behavior of extruded AZ91D magnesium alloy based on SHPB experiments." Chinese Journal of NonferrousMetals 24.08 (2014): 1968-1975. https://doi.org/10.19476/j.ysxb.1004.0609.2014.08.005.

[55] I.G. García, M. Paggi, V. Mantič,Fiber-size effects on the onset of fiber–matrix debonding under transverse tension: A comparison between cohesive zone and finite fracturemechanics models,Engineering Fracture Mechanics,Volume 115,2014,Pages 96-110,ISSN 0013-7944,https://doi.org/10.1016/j.engfracmech.2013.10.014.

[56] Xia Zhou, Wenming Bu, Shangyu Song, Frederic Sansoz, Xiaorun Huang,Multiscale modeling of interfacial mechanical behaviours of SiC/Mg nanocomposites,Materials & Design,Volume 182,2019,108093,ISSN 0264-1275,https://doi.org/10.1016/j.matdes.2019.108093.

[57] Lei Gao, Huimin Kong, Xingkuan Deng, Zhanqi Wang,Multi-scale finite element simulation of asphalt mixture anti-cracking performance,Theoretical and Applied Fracture Mechanics,Volume 121,2022,103490,ISSN 0167-8442,https://doi.org/10.1016/j.tafmec.2022.103490.

[58] Liu, H.W.. Mechanics of materials [M]. Beijing. Higher Education Press.2017.

[59] M. Galli, J. Cugnoni, J. Botsis, J. Janczak-Rusch,Identification of the matrix elastoplastic properties in reinforced active brazing alloys,Composites Part A: Applied Science and Manufacturing,Volume 39, Issue 6,2008,Pages 972-978,ISSN 1359-835X,https://doi.org/10.1016/j.compositesa.2008.03.007.

[60] Liu, H.W.. Mechanics of materials [M]. Beijing. Higher Education Press.2017.

[61] Cui Dangqun. (2005).Analytic and goodness-of-fit tests for logistic curve equations. Mat-hematical Statistics and Management (01), 112-115. https://doi.org/10.13860/j.cnki.sltj.2005.01.020.

[62] Huang BY, Xiao P, Chen KH. New advances in composite materials research (above) [J]. Me

tal World, 2007(2): 46-48

[63]Xie Xia, Yu Jun, Wen Bingquan, et al. Application of composite materials in automobiles [J]. International International Textile Journal, 2010 (12): 56-58, 60

[64]Li Xiaobin, Chen Yue. Properties and applications of metal matrix composites [J]. Thermal Processing Craft, 2006, 35(8): 71-74.

[65]Bralower AF.Moder Casting.1989.（8）:32

[66]Legoux JG.ct alFabrication of Particulates Reinforced Metal Comnposites Pro Conf.1990.Canada. 101

[67]Liu H.ASF Trans.1993,（102）:769

[68]ThomasF Klimowicz JOM.1994.（11）:49

[69]David M.JOM,1993.（5）:26

[70]Zhai Chunquan, Liu Liufa, Jiang Haiyan, Yao Zhendi. Labor protection and disaster control in aluminum-magnesium alloy casting production process[J]. Casting Technology,2008,29(12):1630-1633.

[71]Lewis Robert K. Radon in the Workplace: the Occupational Safety and Health Administration (OSHA) Ionizing Radiation Standard.[J]. Health physics,2016,111(4).

[72]Dudley Susan E,Morriss Andrew P. Will the Occupational Safety and Health Administration's Proposed Standards for Occupational Exposure to Respirable Crystalline Silica Reduce Workplace Risk?[J]. Risk analysis : an official publication of the Society for Risk Analysis,2015,35(7).

[73]Risk Analysis; Report Summarizes Risk Analysis Study Findings from George Washington University (Will the Occupational Safety and Health Administration's Proposed Standards for Occupational Exposure to Respirable Crystalline Silica Reduce Workplace Risk?)[J]. Politics & Government Week,2016.

[74]Brent C. Faulkner,David B. Drake,Andrew J.L. Gear,Frederick H. Watkins,Richard F. Edlich. Molten metal burns: Further evidence of industrial foundries' failure to comply with occupational safety and health administration regulations[J]. Journal of Emergency Medicine,1997,15(5).

[75]Park Sungwon,Johnson Michael D,Hong OiSaeng. Analysis of Occupational Safety and Health Administration (OSHA) noise standard violations over 50 years: 1972 to 2019.[J]. American journal of industrial medicine,2020,63(7).

[76]Zhang LH, Deng B, Wang DY, Deng UK. A case-control study of acute CO poisoning follo

wed by venous thromboembolism[J]. Industrial Hygiene and Occupational Diseases,2022,48(05):392-395.DOI:10.13692/j.cnki.gywsyzyb.2022.05.012.

[77] Wan Chunyan,Zhang Yuchao. Effect of pre-hospital and in-hospital seamless integrated emergency care model in the care of patients with acute CO poisoning[J]. Health Care Medicine Research and Practice,2022,19(07):93-97.

[78] Scott D H T. Fire safety and emergency evacuation guidelines.[J]. Anaesthesia,2021,76(11).

[79] Ji Jie,Hamins Anthony,Hostikka Simo,Jangi Mehdi,Tanaka Futoshi,Ding Long. Fire safety of complex buildings (tall buildings, tunnels, subways, etc.)[J]. Building Simulation,2022,15(4).

APPENDIX

The RSA stochastic algorithm program:

```
def liangxian(point1,point2,point3,point4):
    sign = True
    dis = point[2]
    k1 = (point2[1]-point1[1])/(point2[0]-point1[0])
    b1 = point1[1]-point1[0]*k1
    k2 = (point4[1]-point3[1])/(point4[0]-point3[0])
    b2 = point3[1]-point3[0]*k2
    pp1 = point3[0]*k1+b1
    pp2 = point4[0]*k1+b1
    pp3 = point1[0]*k2+b2
    pp4 = point2[0]*k2+b2
    pd1 = pp1-point3[1]
    pd2 = pp2-point4[1]
    pd3 = pp3-point1[1]
    pd4 = pp4-point2[1]
    ppdd1=pd1*pd2
    ppdd2 =pd3*pd4
    if ppdd1<=0 and ppdd2<=0:
        sign = False
    return sign
```

```
def panduan(point,points):
    sign1 = True
    for jjj in points:
        for ij in range(point[-1]):
            for iii in range(jjj[-1]):
                point1 = point[ij]
                if ij!=point[-1]-1:
                    point2 = point[ij+1]
                else:
                    point2 = point[0]
                point3 = jjj[iii]
                if iii!=jjj[-1]-1:
                    point4 = jjj[iii+1]
                else:
                    point4 = jjj[0]
                if  liangxian(point1,point2,point3,point4)==False:
                    sign1 = False
                    break
            if sign1==False:
                break
        if sign1==False:
```

```
            break
    return sign1


def neiwai(point,length,width):
    sign2 = True
    for dian in range(point[-1]):
        if point[dian][0]>=length or point[dian][0]<=0:
            sign2 = False
            break
        if point[dian][1]>=width or point[dian][1]<=0:
            sign2 = False
            break
    return sign2
def panduan2(point,points):
    sign3 = True
    for bao in points:
        dis = sqrt((point[-2][0]-bao[-2][0])**2.0+(point[-2][1]-bao[-2][1])**2.0)
        if dis<=point[-2][-1] or dis<=bao[-2][-1]:
            sign3 = False
            break
    return sign3
```

```
def fibd(points,fiber):
    sign4 = True
    point1 = fiber[0]
    point2 = fiber[1]
    for xiaobian in points:
        for dangen in range(xiaobian[-1]):
            dis1 = sqrt((point1[0]-xiaobian[-2][0])**2+(point1[1]-xiaobian[-2][1])**2)
            dis2 = sqrt((point2[0]-xiaobian[-2][0])**2+(point2[1]-xiaobian[-2][1])**2)
            if dis1<=0.9*xiaobian[-2][-1] or dis2<=0.9*xiaobian[-2][-1]:
                sign4 = False
                break
            point3 = xiaobian[dangen]
            if dangen!=xiaobian[-1]-1:
                point4 = xiaobian[dangen+1]
            else:
                point4 = xiaobian[0]
            if liangxian(point1,point2,point3,point4)==False:
                sign4 = False
                break
        if sign4==False:
            break
    return sign4
```

```
def onlfib(fiber,fibers):
    sign5 = True
    point1 = fiber[0]
    point2 = fiber[1]
    for qianf in fibers:
        point3 = qianf[0]
        point4 = qianf[1]
        if liangxian(point1,point2,point3,point4)==False:
            sign5 = False
            break
    return sign5


def judge11(points,point):
    sign = True
    xx1 = point[0][0]
    yy1 = point[0][1]
    xy1 = point[1][0]
    yz1 = point[1][1]
    for jiedian in points:
        for iji in range(21):
            for jij in range(21):
                xx2 = jiedian[0][0]
```

```
                yy2 = jiedian[0][1]
                xy2 = jiedian[1][0]
                yz2 = jiedian[1][1]
                DID = sqrt((xx1+iji*(xy1-xx1)/20.0-xx2-jij*(xy2-
xx2)/20.0)**2+(yy1+iji*(yz1-yy1)/20.0-yy2-jij*(yz2-yy2)/20.0)**2)
                if DID<=2.5:
                    sign = False
                    break
            if sign == False:
                break
        if sign == False:
            break
    return sign
length,width,= getInputs(
   fields=(('length:', '100.00'),('width:', '100.00')),label='Base',dialogTitle='Enter
information.')
num_min,num_max,bian_min,bian_max,jiemian,contents= getInputs(
   fields=(('num_min:', '3'),('num_max:', '20'),('bian_min:', '3.0'),('bian_max:',
'4.0'),('jiemian:(0/1)', '0'),('contents:', '0.40')),label='GULIAO',dialogTitle='Enter
information.')
length_min,length_max,fiber_number= getInputs(
   fields=(('fiber_length_min:', '5.0'),('fiber_length_max:', '10.0'),('fiber_number:',
```

```
'100')),label='Fiber',dialogTitle='Enter information.')
length = float(length)
width = float(width)
num_min = int(num_min)
num_max = int(num_max)
bian_min = float(bian_min)
bian_max = float(bian_max)
length_min = float(length_min)
length_max = float(length_max)
fiber_number = int(fiber_number)
jiemian = int(jiemian)
contents = float(contents)
if jiemian==1:
    tjiemian_min,tjiemian_max= getInputs(
        fields=(('t_min:', '0.1'),('t_max:', '0.2')),label='jiemian',dialogTitle='Enter information.')
    tjiemian_min = float(tjiemian_min)
    tjiemian_max = float(tjiemian_max)
    pointnei = []

# 初始化模型
if mdb.models.has_key("Model-1"):
```

```
    myModel = mdb.models["Model-1"]
else:
    myModel = mdb.Model(name="Model-1", modelType=STANDARD_EXPLICIT)

# 画基体
s = myModel.ConstrainedSketch(name='__profile__', sheetSize=200.0)
g, v, d, c = s.geometry, s.vertices, s.dimensions, s.constraints
s.rectangle(point1=(0.0, 0.0), point2=(length, width))
p = myModel.Part(name='Base', dimensionality=TWO_D_PLANAR, type=DEFORMABLE_BODY)
p = myModel.parts['Base']
p.BaseShell(sketch=s)
s.unsetPrimaryObject()
del myModel.sketches['__profile__']
S_base = length*width
S_inner = 0.0

#画多边形
points = []
n = 0
if contents>0:
    while True:
```

```
pd = 0
if jiemian==1:
    t_jiemian = random.uniform(tjiemian_min, tjiemian_max)
num =    random.randint(num_min, num_max)
radius = random.uniform(bian_min, bian_max)
disx = random.uniform(0,length)
disy = random.uniform(0,width)
jiao = 3.1415926*2.0/float(num)
tt = 1.0
point = []
pointnn = []
for i in range(num):
    tt1 = random.uniform(0.9*tt,tt)
    jiaodu = random.uniform(float(i)*jiao,float(i+1)*jiao)
    p11x = tt1*radius*cos(jiaodu)+disx
    p11y = tt1*radius*sin(jiaodu)+disy
    if jiemian==1:
        p11xw = tt1*(radius+t_jiemian)*cos(jiaodu)+disx
        p11yw = tt1*(radius+t_jiemian)*sin(jiaodu)+disy
        point.append((p11xw,p11yw))
        pointnn.append((p11x,p11y))
    else:
```

```
                point.append((p11x,p11y))
        if jiemian==1:
            point.append((disx,disy,radius+tjiemian_min))
            pointnn.append((disx,disy,radius))
            pointnn.append(num)
        else:
            point.append((disx,disy,radius))
        point.append(num)
        if len(points)==0 and neiwai(point,length,width):
            pd = 1
        elif panduan(point,points) and neiwai(point,length,width) and
panduan2(point,points):
            pd = 1
        if pd==1:
            points.append(point)
            if jiemian==1:
                pointnei.append(pointnn)

            for mian in range(num):
                if mian!=num-1:
                    S_MIANJI =
0.5*(disx*point[mian][1]+point[mian][0]*point[mian+1][1]+point[mian+1][0]*disy-
```

```
disx*point[mian+1][1]-point[mian][0]*disy-point[mian+1][0]*point[mian][1])
                    S_inner = S_MIANJI + S_inner
                else:
                    S_MIANJI = 0.5*(disx*point[mian][1]+point[mian][0]*point[0][1]+point[0][0]*disy-disx*point[0][1]-point[mian][0]*disy-point[0][0]*point[mian][1])
                    S_inner = S_MIANJI + S_inner
            content = S_inner/S_base
            print '----{}%----'.format(100.0*content/contents)
            if content>=contents:
                break


    mysketch_2 = mdb.models['Model-1'].ConstrainedSketch(name='__profile__', sheetSize=200.0)
    mysketch_2.setPrimaryObject(option=STANDALONE)
    for hua in points:
        for gehsu in range(hua[-1]):
            if gehsu!=hua[-1]-1:
                mysketch_2.Line(point1=hua[gehsu], point2=hua[gehsu+1])
            else:
                mysketch_2.Line(point1=hua[gehsu], point2=hua[0])
    myPart2 = myModel.Part(name='RVE', dimensionality=TWO_D_PLANAR,
```

```
type=DEFORMABLE_BODY)
    myPart2.BaseShell(sketch=mysketch_2)
    del mdb.models['Model-1'].sketches['__profile__']
    if jiemian==1:
        mysketch_2 = mdb.models['Model-1'].ConstrainedSketch(name='__profile__',
sheetSize=200.0)
        mysketch_2.setPrimaryObject(option=STANDALONE)
        for hua in pointnei:
            for gehsu in range(hua[-1]):
                if gehsu!=hua[-1]-1:
                    mysketch_2.Line(point1=hua[gehsu], point2=hua[gehsu+1])
                else:
                    mysketch_2.Line(point1=hua[gehsu], point2=hua[0])
        myPart2 = myModel.Part(name='JIEMIAN', dimensionality=TWO_D_PLANAR,
type=DEFORMABLE_BODY)
        myPart2.BaseShell(sketch=mysketch_2)
        del mdb.models['Model-1'].sketches['__profile__']
#画纤维
fibers = []
if fiber_number>0:
    num = 0
    while True:
```

```
    jma = 0
    fibre_length = random.uniform(length_min, length_max)
    x = random.uniform(0, length)
    y = random.uniform(0, width)
    angle_z = random.uniform(0, 2*3.1415926)
    x2 = x + fibre_length*cos(angle_z)
    y2 = y + fibre_length*sin(angle_z)
    if x2>0 and x2<length:
        if y2>0 and y2<width:
            fiber = ((x,y), (x2,y2),fibre_length)
            if len(fibers)==0 and fibd(points,fiber):
                jma = 1
            elif onlfib(fiber,fibers) and fibd(points,fiber) and judge11(fibers,fiber):
                jma =1
    if jma==1:
        fibers.append(fiber)
        num+=1
        print '*****Fiber----{}****'.format(num)
        if num==fiber_number:
            break

if fiber_number>0:
```

```
        s = myModel.ConstrainedSketch(name='__profile__', sheetSize=200.0)
        g, v, d, c = s.geometry, s.vertices, s.dimensions, s.constraints
        for fiber in fibers:
            s.Line(point1=fiber[0], point2=fiber[1])
        p = myModel.Part(name='Fiber', dimensionality=TWO_D_PLANAR,
type=DEFORMABLE_BODY)
        p.BaseWire(sketch=s)
        s.unsetPrimaryObject()
        del myModel.sketches['__profile__']

if contents>0:
    myAssembly = myModel.rootAssembly
    myAssembly.DatumCsysByDefault(CARTESIAN)
    myAssembly.Instance(name='Base-1', part=myModel.parts['Base'], dependent=ON)
    if jiemian==0:
        myAssembly.Instance(name='RVE-1', part=myModel.parts['RVE'], dependent=ON)
        myAssembly.InstanceFromBooleanCut(name='R_BASE',
             instanceToBeCut=myAssembly.instances['Base-1'],
             cuttingInstances=(myAssembly.instances['RVE-1'], ),
originalInstances=DELETE)
    elif jiemian==1:
        myAssembly.Instance(name='JIEMIAN-1', part=myModel.parts['JIEMIAN'],
```

```
dependent=ON)
    myAssembly.InstanceFromBooleanCut(name='R_BASE',
          instanceToBeCut=myAssembly.instances['Base-1'],
          cuttingInstances=(myAssembly.instances['JIEMIAN-1'], ),
originalInstances=DELETE)
    myAssembly.Instance(name='JIEMIAN-1', part=myModel.parts['JIEMIAN'],
dependent=ON)
    myAssembly.Instance(name='RVE-1', part=myModel.parts['RVE'], dependent=ON)
    myAssembly.InstanceFromBooleanMerge(name='RVE_JI', instances=(
          myAssembly.instances['JIEMIAN-1'], myAssembly.instances['RVE-1'], ),
keepIntersections=ON,
          originalInstances=DELETE, domain=GEOMETRY)
    del myAssembly.features['RVE_JI-1']
    del myModel.parts['RVE']
    del myModel.parts['JIEMIAN']
    p = myModel.parts['RVE_JI']
    f = p.faces
    faces = []
    for jihe in points:
        zhaomian1 = f.findAt(((jihe[-2][0],jihe[-2][1], 0.0), ))
        jiaobiao1 = zhaomian1[0].index
        if faces==[]:
```

```
                faces = f[jiaobiao1:jiaobiao1+1]
            else:
                faces = faces+f[jiaobiao1:jiaobiao1+1]
        p.Set(faces=faces, name='GULIAO')
    del myAssembly.features['R_BASE-1']
    del myModel.parts['Base']
```